Journal of Computational Physics (2022)

Contents lists available at ScienceDirect

Journal of Computational Physics

journal homepage: www.elsevier.com/locate/jcp

Analysis and design of a local time stepping scheme for LES acceleration in reactive and non-reactive flow simulations*

Sreejith N. A.[a,*], Eleonore Riber[a], Bénédicte Cuenot[a]

[a] *CERFACS, 42 Avenue Gaspard Coriolis, Toulouse Cedex 01, 31057, France*

ARTICLE INFO

Article history:

Keywords: local time-stepping, domain-decomposition, explicit time integration, LES, spectral analysis

ABSTRACT

Explicit time integration based CFD solvers suffer from restriction on the maximum allowable time step computed from the well known Courant-Friedlich-Lewy (CFL) stability criterion. This restriction poses severe challenge in carrying out large eddy simulation (LES) of reactive and non-reactive flows, where the grid resolution is fine. The challenge of restricted time step is further augmented when dealing with large computational domains that pose a wide disparity in the system time scales. In this study, a numerical methodology is presented based on local time stepping in an overset grid framework. The attainable speedup is found to be a function of the ratio of time steps used in the sub-domains and the ratio of the number of computational degrees of freedom. The method is analysed using global spectral analysis (GSA) and shows excellent agreement in solution accuracy with the conventional explicit time integration based solver. The impact of local time stepping on the order of accuracy and global conservation properties are also presented. This method is then applied to simulate three flow test cases to demonstrate the ability of the method to reproduce the first and second-order turbulent statistics at reduced computational time.

1. Introduction

Today, LES is slowly replacing RANS (Reynolds-Averaged Navier-Stokes) based CFD solvers as an industrial design tool [1]. However, explicit time integration based LES solvers still suffer from numerical challenges that prevent their use in scenarios where wide spatial and temporal scale separation exists, such

*

*Corresponding author. Tel.: +33-0621891101;
e-mail: sreejith.na@gmail.com (Sreejith N. A.)

as in external aerodynamics, plume simulations in forest fires and in huge industrial devices. The only drawback that restricts applicability of LES computations in such scenarios is the high computational cost associated with it in comparison to RANS. While this is partly because of the fine grid resolution (and hence the high cell count) demanded by LES computations, the major limitation arises from the restriction on the maximum allowable time step that can be chosen for time integration of the unsteady LES governing equations. The maximum allowable time step is determined by stability requirements of the numerical scheme, popularly known as the CFL criterion. Such a time step restriction is mandatory if the scheme has to be numerically stable and even more restrictive if it must be dispersion-relation preserving. Many studies have been carried out in the past to address these particular aspects. They are briefly described as follows.

A common approach is to use implicit and implicit-explicit (IMEX) time integration schemes. In implicit schemes, the residual in the difference equation is expressed as a function of flow variables at the $(n+1)^{\text{th}}$ time level. From Von-Neumann stability analysis, many authors have concluded that this method gives unconditional stability and that large values of the CFL number (N_c) can be used in such computations. Here, N_c is defined as $N_c = c\Delta t/h$ where $c, \Delta t$ and h are the characteristic velocity, time step and grid size respectively. Such a 'theoretical unconditional stability' comes at an increased computational cost. This is due to the need for the solution of a system of linear algebraic equations for the unknown dependent variables at time level $n+1$ using direct or iterative solvers. The solution of these linear equations also negatively impacts the parallelizability of the solver. Additionally, the unconditional numerical stability is seldom achieved in practical computations. In [2], the authors have carried out LES of turbulent channel flow and have concluded that the ratio of the time step calculated in each cell and the cell characteristic length should not be more than $2-3$, thus effectively limiting the maximum allowable time step that can be chosen even in implicit schemes. Another drawback of implicit schemes is their poor numerical resolution properties compared to explicit schemes. In [3], authors have carried out DNS of transitional flow over a flat plate with monochromatic wall excitation using implicit and explicit schemes. Their study concluded that even though the implicit scheme used in their analysis enjoyed neutral stability, it could not predict the spatio-temporal wave front typically observed in flows en route to turbulence. IMEX methods perform even worse since, in addition to the above-mentioned aspects, the interface between the implicit and explicit time integration zones could act as source of erroneous wave packets [3].

On the other hand, in the case of explicit time integration schemes, the solution at the $(n+1)^{\text{th}}$ time level depends only on the current and previous time levels. Hence, this class of schemes does not require the complicated matrix inversion procedure and is computationally cheap. They also enjoy the benefits of efficient parallelizability and excellent accuracy and resolution properties. Many modifications of explicit schemes, with the objective of surmounting the CFL stability criteria have been developed in the past and can be broadly classified as asynchronous methods, multirate schemes and domain decomposition-based local time stepping schemes.

Recently, an asynchronous method [4] was developed for unsteady equations using the 'discrete-event

simulation' methodology. In this method, a timestamp is associated with each computational cell in the domain based on a predicted "event" described by the governing PDE. This step is followed by an event processing step where the cell with the smallest time stamp is time-integrated using the maximum allowable time step in that cell. This is in turn followed by an event synchronization step where the cell neighboring the smallest timestamp cell is updated and flux interfaces are corrected. Finally, an event scheduling step is initiated where the time stamp and the residual of the cell is recalculated. The above procedures are repeated for all cells in the domain to calculate the unsteady solution. The authors have proved the stability of this method and demonstrated its application to 1D convection-diffusion-reaction equation. In [5, 6, 7, 8], other authors have extended this approach by applying the local CFL number N_c as refreshing time stamps and demonstrated the method for gas discharge problems. The authors of another study [9] have devised yet another asynchronous method using first-order upwind schemes. The issue of conservation is addressed in that work by carrying out flux interpolation at cell interfaces with different local time steps. In their work, the authors have demonstrated the applicability of this methodology to aeroacoustic problems. Similarly, the application of asynchronous method to gas dynamics equations is detailed in [10, 11].

Adaptive mesh refinement (AMR) methods fall into the category of both asynchronous methods as well as multirate schemes. AMR schemes were introduced through the pioneering work of Berger [12]. In their work which used block structured meshes, the global mesh comprises a 'parent' coarse mesh and several 'children' fine meshes overlapping with the parent mesh. Local time steps are used to time-integrate the finer children meshes. In effect, this method introduces both spatial and temporal adaptivity. The parent mesh solution values located inside the child mesh are then obtained by volume-weighted averaging of the finer children mesh solution located inside the parent mesh. The flux values at the parent-children interface are also obtained by interpolating solution values from the child mesh. This method of Berger was then extended to include coincident parent-children mesh interface to ensure global conservation in [13] in a finite difference framework. A similar approach applied to a finite element framework is explained in [14]. In [15, 16, 17, 18], the AMR approach was applied to solve incompressible Navier-Stokes equations using projection method. In another attempt [19], the same approach was extended to study two-phase flows with level set and surface tension methods.

In multirate time integration schemes, multiple time steps are present in the computational domain and each time step is devoted to a group of contiguous cells. The time steps are chosen such that they are integral multiples of the smallest time step in the domain. One of the early attempts at multirate schemes is the work of Osher and Sanders [20]. In this work, the authors established a locally varying time step for forward Euler time integration schemes for various flux functions. However, their schemes were first-order accurate in space and time. In [21], the authors extended this work to second-order schemes in space and time. However, their scheme is not mass conservative. Similar second-order schemes were also developed in [22, 23]. These schemes, like the one designed in [21], are found to be non-conservative in nature. Extension of these methods to third-order [24, 25] and fourth-order accuracy [26, 27] also has been carried out recently.

Domain decomposition methods using local time stepping work on similar lines as multirate schemes, the only difference being that the full computational domain is divided into multiple overlapping sub-domains with each sub-domain being time-integrated using a time step specific to that particular sub-domain. Like multirate schemes, each time step in the sub-domain is chosen as an integral multiple of the smallest time step. This approach has been used in [28] to model cardiac tissues. The application of this method to CFD is discussed in [29]. In that work, the authors have developed a domain decomposition-based local time stepping method for various explicit numerical schemes. This method is then applied to the LES of a 2-dimensional jet flow as a validation exercise. The same method has been applied to the LES of plume from a rocket nozzle in [30].

In summary, multiple approaches have been devised to tackle the challenge of numerical stiffness in LES. Although implicit methods guarantee 'theoretical stability' for all N_c values, the maximum N_c value that can be often used is restricted in LES. The computational cost of matrix inversion and poor numerical resolution has also demonstrated drawbacks of implicit methods. On the other hand, explicit methods have good resolution properties and parallelizability but suffer from stringent stability conditions. Asynchronous time stepping methods, used to improve this stability restriction have been attempted in the past but their applicability to LES is still not demonstrated. Multirate schemes and AMR schemes are often limited to structured block grids. Domain decomposition methods, on the other hand, are applicable to unstructured grids and have the advantages enjoyed by multirate schemes.

Hence in this study, an extension of the domain decomposition method in [29] is proposed. In [29], the authors introduce a domain-decomposition based local time-stepping method named Deccoup. The method is demonstrated using a simple one-dimensional linear PDE with a hyperbolic tangent function used as a filter function in the overlapped zone (terminologies are explained in Section 4). The error in the physical space due to local time-stepping is also reported. However, in the present study, we propose that inorder to keep the computational cost low for multi-dimensional LES simulations, the use of a Heaviside-like filter function would suffice for achieving low numerical errors. We also present a detailed error analysis in the spectral space using Global Spectral Analysis (GSA) of two popular numerical schemes applied to the linear convection equation and validate it using three different flow scenarios and using different types of grid elements. GSA [31] is a spectral analysis tool used to study the properties of numerical schemes while also including the effect of boundary stencils. GSA has been used to study Dispersion Relation Preservation (DRP) schemes [32] used for DNS and LES of incompressible [33] and compressible flows [34]. The application of GSA to the study of numerical schemes used for non-uniform grids [35, 36] and for domain-decomposition based methods ([37, 38]) has been demonstrated in the past. While GSA of the linear convection-diffusion [39] and convection-diffusion-reaction [40] equation are already available in the literature, for the sake of brevity, we restrict our analysis of the proposed method to the linear convection equation only. For the extension of the analysis to linear convection-diffusion equation, readers may refer to [41].

This paper is organized as follows. The method, hereafter referred to as the LESAULTS (acronym for LES acceleration using local time stepping) method, is described in detail in Section 2. The theoretical speedup limit that can be attained using LESAULTS method is described in Section 3. The detailed design aspects of the method are elucidated in Section 4 followed by its error analysis using GSA in Section 5. The method is then validated using numerical tests and the details of the results are provided in Section 6. The conclusions and perspectives from this work are listed in Section 7.

2. LESAULTS Method

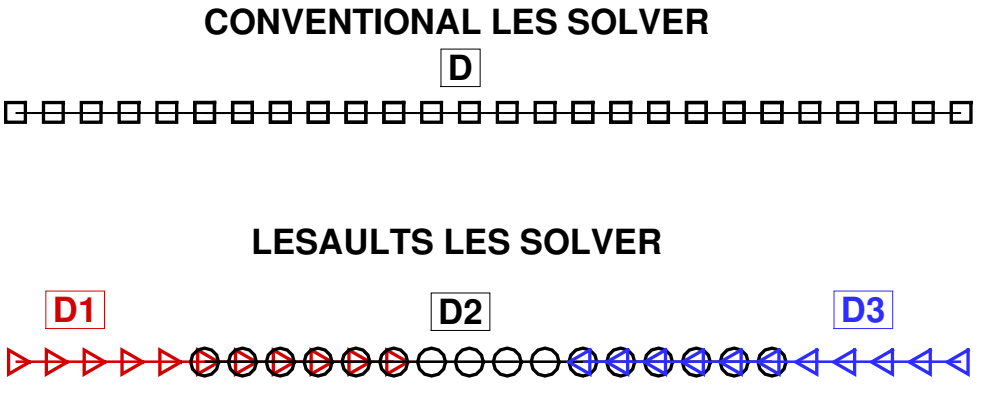

(a) Conventional and LESAULTS domains in 1D

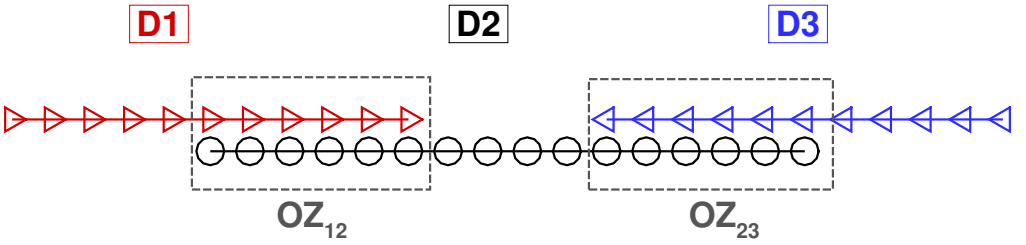

(b) LESAULTS domains and the overlapped regions

Fig. 1: Schematic of conventional and LESAULTS method applied to a 1D domain. (a) single domain used in conventional solver and sub-domains used in LESAULTS method. (b) An exaggerated view of overlapped zones

To describe the LESAULTS method, a simplified, one-dimensional computational domain as shown in Fig. 1 is considered. At this point no assumption is made on the nature or type of the unsteady governing equation(s). Let the one-dimensional domain D (colored in black) shown in Fig. 1(a) be used to calculate the solution using the conventional explicit solver. It is assumed that the domain D is discretized using N_{conv} number of nodes shown as square symbols in the figure. The grid spacing in the domain can be uniform or spatially varying.

In LESAULTS method, the domain D is decomposed into three overlapping sub-domains-$D1$,$D2$ and $D3$ such that $D = D1 \cup D2 \cup D3$. The overlapped zones between the sub-domains are named as OZ12 and

Subdomain, i	Number of nodes, N_i	Max. permissible time step, Δt_i	Number of intermediate integrations, $R_{\delta t,i}$
D1	N_1	Δt_1	$\mathcal{LCM}(\Delta t_i)/\Delta t_1$
D2	N_2	Δt_2	$\mathcal{LCM}(\Delta t_i)/\Delta t_2$
D3	N_3	Δt_3	$\mathcal{LCM}(\Delta t_i)/\Delta t_3$

Table 1: Table showing the sub-domains, time steps and the number of intermediate time integration steps for the LESAULTS configuration shown in Fig. 1

OZ13 such that $OZ12 = D1 \cap D2$ and $OZ23 = D2 \cap D3$. Let the number of nodes in the sub-domains $D1$, $D2$ and $D3$ be N_1, N_2 and N_3 respectively. These numbers include the number of nodes present in the overlapped zones as well. Similarly, the grid spacing in all the three sub-domains can be either uniform or spatially varying. However, to make a fair comparison between the conventional method and LESAULTS method, the grid spacing in the conventional and the corresponding sub-domain is taken to be identical. It is also ensured that the nodes of the two sub-domain meshes located in the overlapped zones have an exact node-to-node conformance in their physical location. Although not mandatory, this assumption is easily enforced since only stationary meshes are considered in this study and it removes the interpolation errors in the solution procedure. Let the number of nodes in $OZ12$ and $OZ23$ be N_{12} and N_{13} respectively. Out of the total number of nodes in the overlapped zones $OZ12$, half of them belong to $D1$ and the other half belong to $D2$. Let the maximum permissible time steps in each of the sub-domains $D1$, $D2$ and $D3$ be Δt_1, Δt_2 and Δt_3 respectively. These values of time steps are assumed to be known a priori. It is evident that the grid size in the overlapped regions $OZ12$ and $OZ23$ are such that they respect the stability criteria for the larger among the two time steps pertaining to each of the two sub-domains constituting the overlapped zones. These details are summarized in Table 1 for further clarity. In the table, $\mathcal{LCM}$ refers to the least common multiple of the time-steps in all the sub-domains.

Here $R_{\delta t,i}$ denotes the number of time integrations the sub-domain i undergoes before reaching the next possible flow time value common to all sub-domains.

The time integration methodology in LESAULTS method comprises two stages namely, (i) the intermediate time integration stage and (ii) the solution synchronization stage. A schematic of an example of these stages is shown in Fig. 2. In the LESAULTS configuration shown in this schematic, the time steps in the sub-domains are given by $\Delta t_1 = 3 \times \Delta t_2 = 2 \times \Delta t_3$. By construction, $R_{\delta t,i} = \mathcal{LCM}(\Delta t_j)/\Delta t_i$ with $\mathcal{LCM}(\Delta t_j) = t^{n+1} - t^n$

Each sub-domain is integrated in time independently of the others, using the time step pertaining to that sub-domain. In the example shown in Fig. 2, $D1$ is integrated once, $D2$ thrice and $D3$ twice. This completes the intermediate time integration stage. It is evident that during this stage, the boundary values at the interface boundaries of each of the sub-domains are unknown. To tackle this shortcoming, they are kept the same as their values at time level t^n, as intermediate Dirichlet boundary conditions.

By the end of the intermediate time integration stage, one obtains a unique solution set for each of

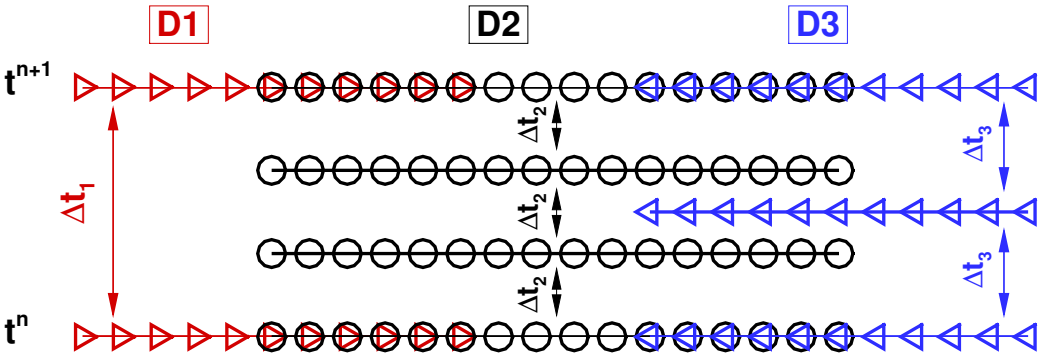

(a) Intermediate time integration stage

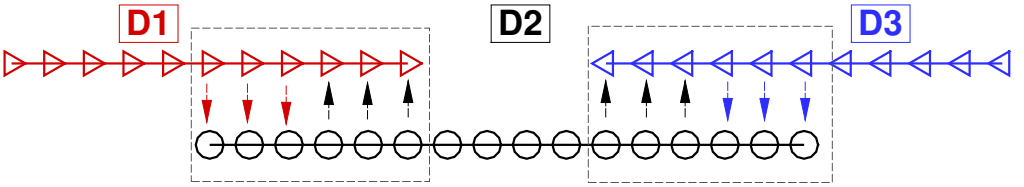

(b) Solution synchronization stage

Fig. 2: Various stages in the LESAULTS method (a) Intermediate time integration stage (b) Solution synchronization stage

the sub-domains. Two sets of solutions are available in the overlapped regions-$OZ12$ and $OZ23$, each one corresponding to the sub-domain to which the mesh node belongs to. This multiplicity of solutions at the same time and spatial location is resolved in the synchronization stage in which a unique solution is computed from the two available solution sets and is imposed in the overlapped zones. This completes the solution synchronization stage.

After both stages, a unique and continuous solution throughout the entire domain is obtained. This completes one stage of the LESAULTS method. The above two steps are repeated to solve for the unsteady solution of governing equations.

3. Theoretical Computational speedup

The speedup obtained using LESAULTS method is defined as the ratio of the computational time taken by the conventional explicit solver to that taken using LESAULTS method for integrating through the same flow time, for the same number of computational degrees of freedom (number of cells/nodes in the mesh) and using the same number of computing cores. Hence, mathematically the theoretical speedup S_{th} is expressed as,

$$S_{th} = \frac{T_{c,CONV}}{T_{c,LESAULTS}}$$

In the above expression, $T_{c,CONV}$ and $T_{c,LESAULTS}$ are the computational times taken by the conventional LES solver and LESAULTS method-based solver respectively.

For a general LESAULTS configuration with N_{sub} number of subdomains and assuming ideal load balancing, the above expression can be derived as,

$$S_{th} = max(R_{\delta t,i}) \frac{(\sum_{i=1}^{N_{sub}} N_i - (\sum_{j=1}^{N_{sub}} \sum_{i=1}^{N_{sub}} N_{ij})/2)}{\sum_{i=1}^{N_{sub}} R_{\delta t_i} N_i} \tag{1}$$

where N_{ij} denotes the number of nodes in the overlapped zones between sub-domains i and j.

The optimum number of cores C_i to be dedicated to sub-domain i for proper load balancing is given by,

$$C_i = \frac{R_{\delta t,i} N_i}{\sum_{i=1}^{N_{sub}} R_{\delta t_i} N_i} C_{tot} \tag{2}$$

where C_{tot} is the total number of cores.

It can be observed from Equation 1 that the speedup S_{th} is maximum when $max(R_{\delta t,i})$ is large along with low values of N_i for sub-domains with $R_{\delta t,i} >> 1$. It should also be emphasized that the number of nodes in the overlapped regions should also be kept as low as possible to achieve the maximum speedup.

To further explain the above expression, we consider a two sub-domain configuration with the larger sub-domain containing larger number (N_1) of nodes having an $R_{\delta t,1}$ value of 1 and the smaller sub-domain containing N_2 number of nodes ($N_2 << N_1$). Then, S_{th} can be expressed as a function of the node number ratio, $R_n = N_1/N_2$ and $R_{\delta t} = R_{\delta t,2}$ as,

$$S_{th} = R_{\delta t} \frac{(R_n + 1)}{(R_n + R_{\delta t})} \tag{3}$$

The variation of S_{th} with R_n and $R_{\delta t}$ is plotted in Fig. 3.

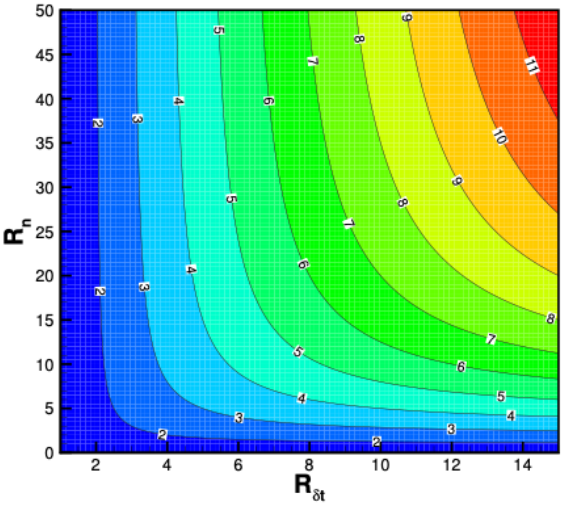

Fig. 3: Contours of S_{th} as a function of R_n and $R_{\delta t}$ for a two sub-domain decomposition

It is observed from Fig. 3 that the speedup is maximum for high values of R_n and $R_{\delta t}$, i.e., for a high value of $R_{\delta t}$ and a small number of nodes in the sub-domain with the smallest time step. Hence, LESAULTS method is efficient in LES computations when the limiting time step is dictated only by a very small number of cells in the computational domain. It should also be emphasized the method in its present form requires an a priori knowledge of the time steps in all the sub-domains.

4. Design of LESAULTS method

The intermediate time integration steps do not require any additional correction in the non-overlapped zones of the sub-domains and are hence carried out in the same way as done for the conventional time integration method. In the overlapped zones, two sets of solutions are obtained after the intermediate time integration stages. In general, these two solution sets are not identical due to the difference in the time steps (CFL numbers) used in the time integration stages and due to the intermediate Dirichlet boundary conditions at the interface boundaries. To enforce a unique solution, the solution synchronization step sketched in Fig. 4 is used.

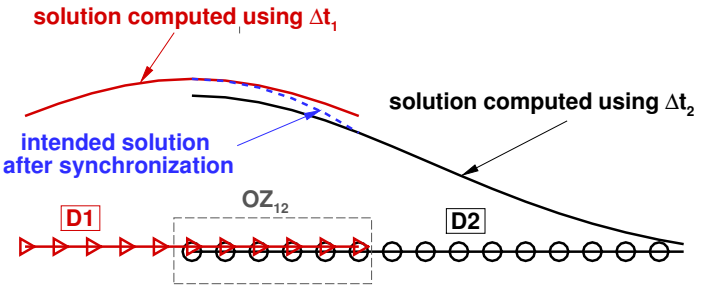

Fig. 4: Solution after intermediate time integration stages and the solution synchronization stage for a 2 sub-domain LESAULTS configuration

The synchronized solution should obey the following criteria:

- The synchronized solution is a function of the solution sets from both subdomains
- It should smoothly blend with the solutions in the sub-domains (as shown in Fig. 4)
- The synchronization should involve a minimum number of nodes in the overlapped zone so that the speedup is maximized
- The erroneous solution at the nodes near to the interface boundaries should be discarded in the synchronization procedure

In order to elucidate the last point in the above list, consider the solution of the linear convection equation on a one-dimensional domain with a Gaussian profile as the initial solution as shown in Fig. 5. In this example, and for the rest of this paper, the following notation is used: ${}^{it}_{l}u^n_j$ is used to denote any

quantity u at the jth node in the lth sub-domain at time level n. The kth intermediate time integration stage after nth time level is referred as $n + k/R_{\delta t}$ where $R_{\delta t}$ is the number of intermediate stages. The left superscript it denotes that the quantity is obtained after intermediate time integration stage. Similarly, for indicating that the quantity is obtained after the solution synchronization stage, a left superscript of ss is used.

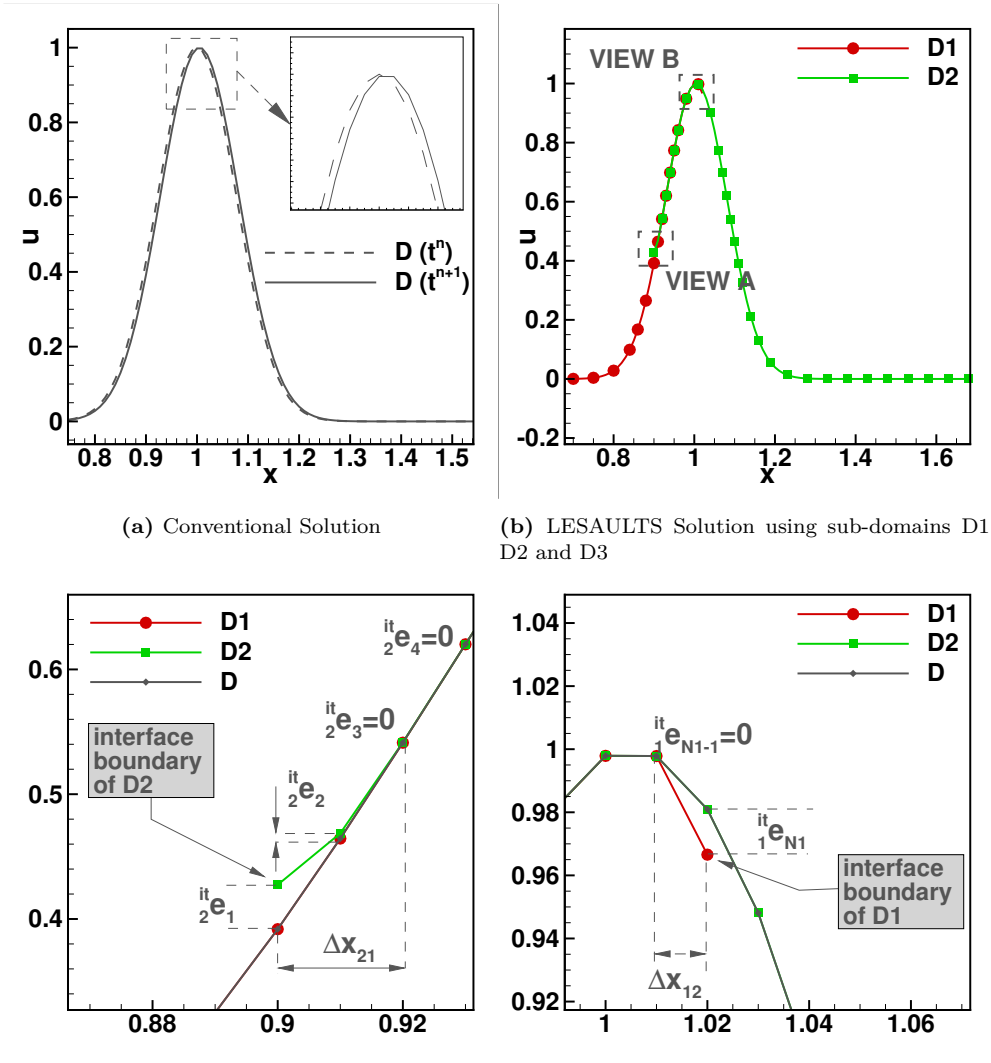

(a) Conventional Solution

(b) LESAULTS Solution using sub-domains D1, D2 and D3

(c) Error near D2 interface boundary (VIEW A) **(d)** Error near D1 interface boundary (VIEW B)

Fig. 5: The evolution of solution after intermediate time integration stage. (a) and (b) shows the solution in conventional and an equivalent LESAULTS domains. (c) and (d) show the error at near boundary nodes due to Dirichlet boundary conditions.

The numerical solution computed on a conventional domain D, at two successive time instants is shown in Fig. 5(a). The corresponding numerical solution obtained after the intermediate time integration stages using a 2 sub-domain LESAULTS method applied to the same problem is shown in Fig. 5(b). The left sub-domain D1 is colored in red while the other sub-domain D2 is shown in green. Zoomed-in views of the computed solution near the interface boundaries of the sub-domains are shown in Figs. 5(c) and (d).

In these figures, the solution computed using the conventional method (colored in grey) is also shown for comparison. The effect of the intermediate Dirichlet boundary condition is pretty evident from these figures. The error due to the boundary conditions, is maximum at the boundary nodes (${}^{it}_{2}u_1$, ${}^{it}_{1}u_{N1}$ in Figures (c) and (d) respectively) and gradually decreases as one moves to the interior. Hence, the synchronization stage should not consider these near boundary nodes which have erroneous solutions. The extent to which the error propagates to the interior of sub-domain D2 during the intermediate time integration stages is shown as Δx_{21} in Fig. 5(c). The similar distance for sub-domain D1 is shown as Δx_{12} in Fig. 5(d). These distances depend on the numerical scheme used, the CFL number N_c, the non-dimensional wavenumber kh (where k is the Fourier wavenumber of the numerical solution) and the number of intermediate stages the sub-domain undergoes as shall be proved in the coming paragraphs.

Based on the previous discussion, for any two coincident nodes i, j located in the sub-domains D1 and D2 respectively, the solution after the synchronization stage is defined as,

$$ {}^{ss}_{1}u_i{}^{n+1} = {}^{ss}_{2}u_j{}^{n+1} = (1 - H(x - x_H))\, {}^{it}_{1}u_i{}^{n+1} + H(x - x_H)\, {}^{it}_{2}u_j{}^{n+1} \tag{4} $$

-where H is the Heaviside-like function defined at $x = x_H$ located in the overlapped zone and is shown in Fig. 6. It should be emphasized that the authors in [29], used a hyperbolic tangent function in place of the Heaviside-like function used in the present study. The authors of this study are of the opinion that while a hyperbolic tangent function is apt for simple flow scenarios where the overlapped zone extends predominantly in one space dimension, it may not be well suited for multi-dimensional and complex overlapped zone geometries. In the present study, it is demonstrated that the usage of the Heaviside-like function in Eq. 4, provides good accuracy at low computational cost especially when dealing with unstructured meshes. The distances Δx_{21} and Δx_{12} which determine the value of x_H are such that the error from the interface boundaries is minimum (possibly zero).

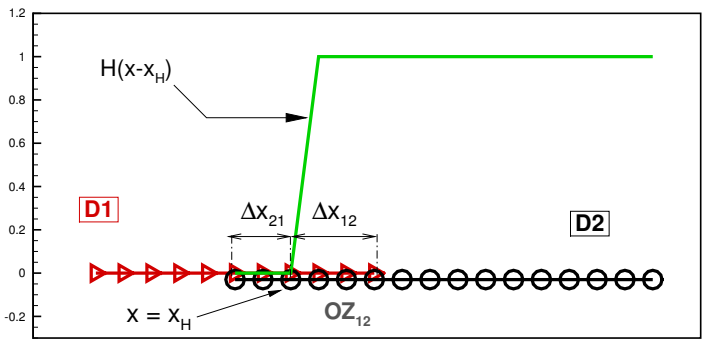

Fig. 6: The definition and location of the Heaviside-like function used in Equation 4

It now remains to determine the value of x_H or equivalently the values of Δx_{21} and Δx_{12} in the example discussed before. This is performed in the following paragraphs.

For this purpose, two popular and widely used numerical schemes, namely Lax-Wendroff([42]) and TTGC ([43]) schemes are used. While Lax-Wendroff (LW) benefits from its low computational cost, TTGC enjoys high accuracy and resolution. For both spatial schemes, the numerical solution after 1 intermediate time integration in sub-domain D2 can be expressed as,

$$[A]\,{}^{it}_{2}\{u\}^{n+1/R_{\delta t,2}} = [B]\,{}^{it}_{2}\{u\}^{n} \tag{5}$$

or,

$${}^{it}_{2}\{u\}^{n+1/R_{\delta t,2}} = [C]\,{}^{it}_{2}\{u\}^{n} \tag{6}$$

with,

$$[C] = [A]^{-1}\,[B] \tag{7}$$

and where $[A]$ is the coefficient matrix which is particular for the numerical scheme under consideration. For the LW scheme, $[A]$ is the identity matrix. For the TTGC scheme [43], which is spatially implicit, the matrix $[A]$ is tridiagonal in nature. $[B]$ is a matrix representing the flux residual computed using the scheme. $\{u\}$ denote the vector of unknown, dependant variables defined at the mesh nodes.

After $R_{\delta t,2}$ intermediate time integration stages, the solution in sub-domain D2 at time level t^{n+1} is given by,

$${}^{it}_{2}\{u\}^{n+1} = [C]^{R_{\delta t,2}}\,{}^{it}_{2}\{u\}^{n} \tag{8}$$

At any particular node i in the sub-domain D2, the above equation can be written as,

$${}^{it}_{2}u_i{}^{n+1} = \sum_{j=1}^{N_2} C_{ij}{}^{R_{\delta t,2}}\,{}^{it}_{2}u_j{}^{n} \tag{9}$$

Here, $C_{ij}{}^{R_{\delta t,2}}$ refers to the $(i,j)^{th}$ element in the matrix $[C]^{R_{\delta t,2}}$.

It is to be noted that since Dirichlet boundary conditions are used at node 1 in sub-domain D2, $C_{11} = 1$ and $C_{1j} = 0$ for $j = 2, 3..N_2$. Expressing the solution ${}_2u_j{}^{n}$ in terms of its Fourier transform one obtains,

$${}^{it}_{2}u_i{}^{n+1} = \sum_{j=1}^{N_2} C_{ij}{}^{R_{\delta t,2}} \int {}_2\hat{U}(k,t^n)\, e^{i\,k\,x_j}\, dk \tag{10}$$

$$= \int \sum_{j=1}^{N_2} C_{ij}{}^{R_{\delta t,2}}\, P_{ji}\;{}_2\hat{U}(k,t^n)\, e^{i\,k\,x_i}\, dk \tag{11}$$

where ${}_2\hat{U}(k,t^n)$ is the Fourier amplitude of the signal ${}_2\{u\}^{n}$.

The matrix P represents a projection operator that projects any dependent variable u from spectral space (k) to real space (x) such that any element (j,i) of matrix P is given by $P_{ji} = e^{i\,kh(j-i)}$. It can be noticed that Eq. 11 introduces the definition of the amplification factor projected at node i and given as,

$$ {}_2G_i{}^{R_{\delta t,2}} = \sum_{j=1}^{N_2} C_{ij}{}^{R_{\delta t,2}}\, P_{ji} \tag{12} $$

It is emphasized that ${}_2G_i{}^{R_{\delta t,2}}$ is in general not the same as derived for a periodic problem. Indeed, the boundary closure scheme introduce deviation near the boundary nodes. This particular aspect has been mentioned in [44].

For the purpose of this paper, the error associated with the LESAULTS method is computed with respect to the solution obtained with the conventional method. By this definition, the error at the boundary node in sub-domain D2 (marked as ${}^{it}_{2}e_1{}^{n+1}$ in Fig. 5)(c) is defined as ${}^{it}_{2}e_1{}^{n+1} = {}^{it}_{2}u_1{}^{n+1} - {}_c u_m{}^{n+1}$ where ${}_c u_m$ refers to the solution computed using conventional method in domain D and m represents the node in domain D that is coincident with that of node 1 in sub-domain D2. Similarly, for any near boundary node i, the error e_i can be expressed as,

$$ {}^{it}_{2}e_i{}^{n+1} = {}^{it}_{2}u_i{}^{n+1} - {}_c u_l{}^{n+1} \; such\; that \tag{13} $$

$$ {}_2x_i = {}_c x_l \tag{14} $$

Expressing ${}^{it}_{2}u_i{}^{n+1}$ and ${}_c u_l{}^{n+1}$ using their Fourier transforms one obtains,

$$ {}^{it}_{2}e_i{}^{n+1} = \int \left[{}_2G_i{}^{R_{\delta t,2}} - {}_c G_{int}{}^{R_{\delta t}} \right] \hat{U}(k, t^n)\, e^{i\,k\,x_i}\, dk \tag{15} $$

In the above equation, the Fourier amplitudes are such that, ${}_2\hat{U} = {}_c\hat{U} = \hat{U}$, since the initial solution applied to domains D and D2 are exactly identical. Also, $R_{\delta t}$ is the number of time integrations that the conventional domain D undergoes from t^n to t^{n+1} and is given by $R_{\delta t} = \mathcal{LCM}(\Delta t_i)/min(\Delta t_i)$.

Here, it is assumed that the node l in domain D is sufficiently far from boundaries and hence the expression for the amplification factor at node l is same as the one evaluated for a periodic domain denoted as ${}_c G_{int}{}^{R_{\delta t}}$ in Eq. 15. The expressions for G_{int} for the Lax-Wendroff (LW) and TTGC schemes are provided in the Appendix. The value of amplification factor at node i, ${}_2G_i{}^{R_{\delta t,2}}$ is evaluated for any particular numerical scheme using Eq. 12. For the analysis, the extreme scenario where $R_{\delta t,2} = R_{\delta t}$ is considered.

A measure of the magnitude of the error ${}^{it}_{2}e_i$ is denoted as $\epsilon_{bnd,i} = |\,{}_2G_i{}^{R_{\delta t,2}} - {}_c G_{int}{}^{R_{\delta t}}|$ and for a given numerical scheme, is a function of the non-dimensional wavenumber kh, CFL number N_c, time step ratio $R_{\delta t,2}$ and the node number, i. To find out the value of $x = x_H$ or equivalently the values of Δx_{21} and Δx_{12}, the value of $\epsilon_{bnd,i}$ is calculated at various nodes near to the boundaries using expression of Eq. 15. The node j at which $\epsilon_{bnd,j}$ is minimum (preferably zero) at a given value of $R_{\delta t,2}$ and for a given scheme is then used to determine $x_H = x_j$.

For the present study, the value of $\epsilon_{bnd,i}$ is calculated by considering the linear convection equation as the governing PDE and for the LW and TTGC schemes. The one-dimensional sub-domain D2 of length 1 units is discretised using 100 linear elements of size $h = 0.01$ and $N_2 = 101$. This is sufficient to ensure

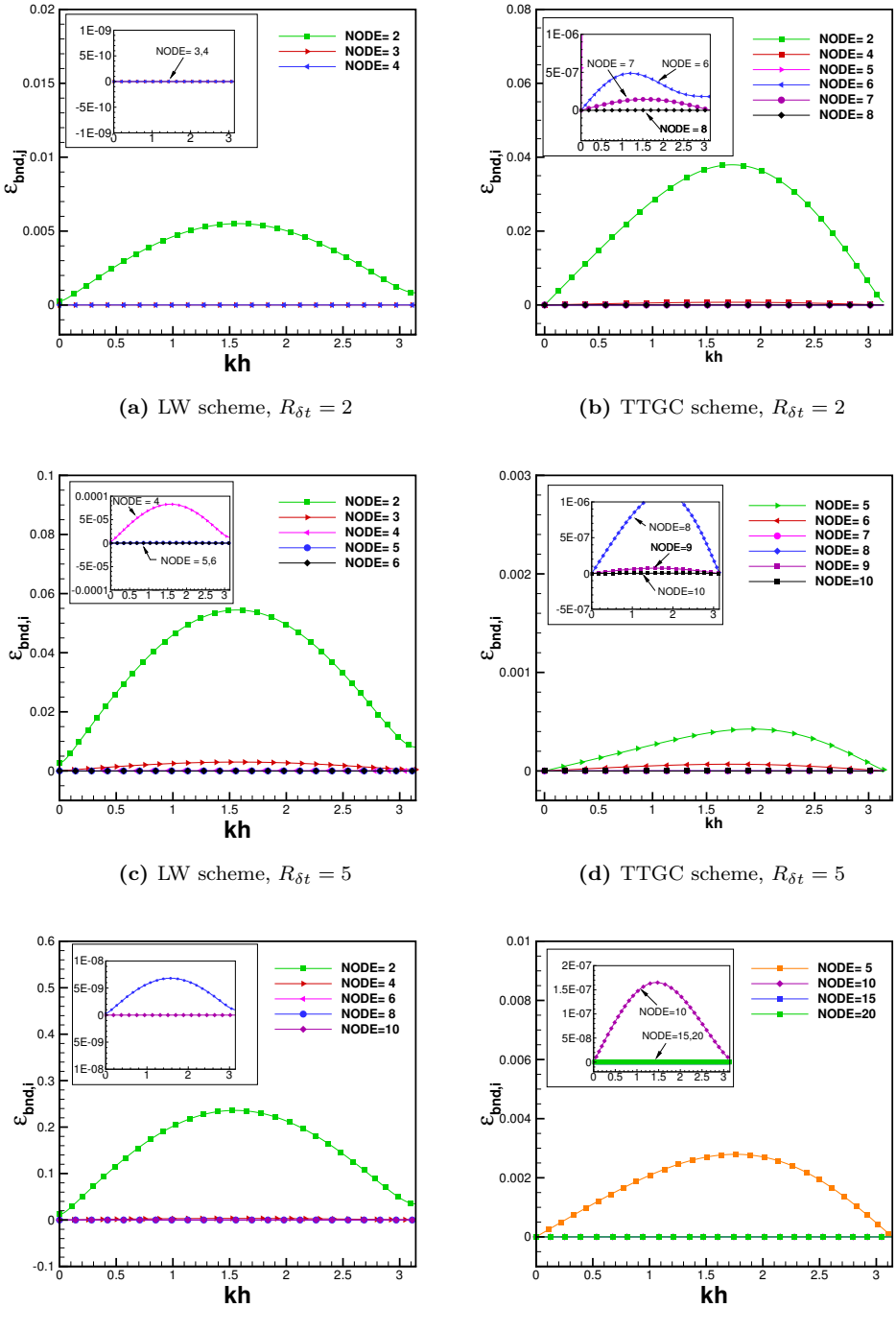

(a) LW scheme, $R_{\delta t} = 2$

(b) TTGC scheme, $R_{\delta t} = 2$

(c) LW scheme, $R_{\delta t} = 5$

(d) TTGC scheme, $R_{\delta t} = 5$

(e) LW scheme, $R_{\delta t} = 10$

(f) TTGC scheme, $R_{\delta t} = 10$

Fig. 7: Variation of $\epsilon_{bnd,i}$ as a function of kh at $N_c = 0.1$ for various nodes near the boundary.

that amplification factor at any interior node approaches the corresponding value calculated for a periodic domain. For the LW scheme, the calculation of $[C]$ is straightforward and is essentially a function of the numerical flux gradient values calculated at every node. For the original TTGC scheme, $[A]$ is tridiagonal in

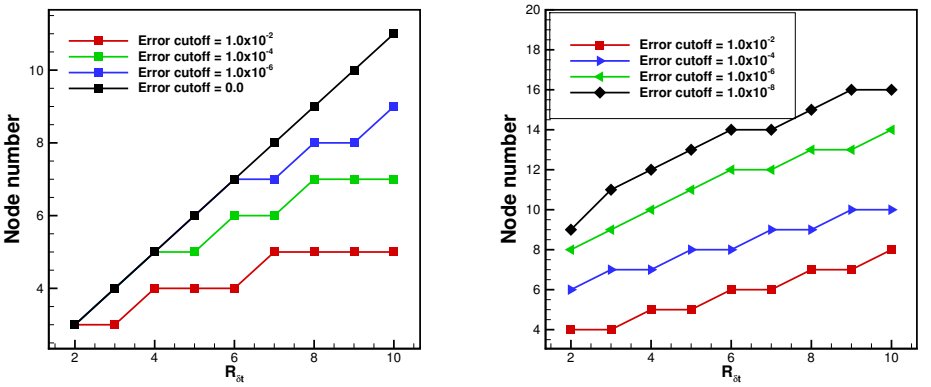

(a) LW scheme **(b)** TTGC scheme

Fig. 8: Node number at which the maximum error is less than or equal to a specified cutoff error plotted for various $R_{\delta t}$ values

nature and the calculation of $[C]$ is computationally intensive. In the numerical implementation of TTGC, an approximate 2-step Jacobi method is used to invert the $[A]$ matrix and is used to calculate the $[C]$ matrix. The details of this Jacobi method is provided in [43].

Fig. 7 shows the value of $\epsilon_{bnd,i}$ plotted at various nodes near the interface boundary for values of $R_{\delta t,2} = 2, 5, 10$. The value of $N_c = 0.1$ is used and $\epsilon_{bnd,i}$ is calculated and plotted across all non-dimensional wavenumbers. One can observe that the value of $\epsilon_{bnd,i}$ is maximum at the near boundary nodes (here i=1 is the boundary node, i=2 is the near boundary node etc.) and reduces as one moves to nodes in the interior of the domain, for both the LW and TTGC schemes. For $R_{\delta t} = 2$ and LW scheme, node 2 produces a maximum error of 0.005 while all the nodes in the interior produce zero error. For the TTGC scheme, absolute zero error is difficult to be obtained due to the implicit nature of the scheme. The error $\epsilon_{bnd,i}$ at node 6 is plotted in the inset in Fig. 7(b) and is found to be of the order 10^{-7}. Similarly, for other values of $R_{\delta t}$, it is observed that the error induced by TTGC scheme is higher than that for LW scheme at the same node. This is due to the spatially implicit nature of the TTGC scheme, which propagates the error of approximate boundary condition farther into the interior of the domain.

In general, it is observed that for the LW scheme, the maximum error falls to absolute zero after the node number $i = R_{\delta t} + 1$. This is observed from Fig. 8 where the nearest boundary node at which the maximum error is less than a specified cutoff value is plotted. For the LW scheme, the error is identically zero for any node $i > R_{\delta t} + 1$. This is because spatially local stencil is used in the LW scheme. For the TTGC scheme, an absolute zero error is difficult to obtain due to the spatially implicit nature of the scheme as mentioned before. Depending on the cut-off error value chosen, the nearest node at which the maximum error is below the specified cut-off value varies. It should also be noted that this particular plot of TTGC is for $N_c = 0.1$. At higher N_c values this value of node number could differ. As a rule of thumb, we propose the node number to be chosen as $2 \times R_{\delta t} + 1$. This would ensure that the error is minimum (although not

zero) and at the same time keep the length of the overlapped zone small. This particular rule is used in the numerical tests which are explained in Section 6 and found to provide accurate results.

Hence, the values of Δx_{21} are determined for both the schemes considered. For the LW scheme, this corresponds to $\Delta x_{21} = (R_{\delta t,2}+1)h$ and similarly for $\Delta x_{12} = (R_{\delta t,1}+1)h$. On the other hand, for the TTGC scheme the corresponding values $\Delta x_{21} = (2R_{\delta t,2}+1)h$ and $\Delta x_{12} = (2R_{\delta t,1}+1)h$ is observed to produce accurate results. Hence, for the overlapped zone OZ_{12}, the optimum number of cells to be used with LW scheme is $R_{\delta t,1} + R_{\delta t,2} + 1$. The corresponding number for TTGC scheme is $2\left(R_{\delta t,1} + R_{\delta t,2}\right) + 1$.

5. Error Analysis

Definition of error: Since the numerical schemes used in this study have been well studied and validated in the past, it is meaningful to study the error arising from LESAULTS with respect to the conventional solver solution rather than the exact solution. Hence, in this study, the error due to LESAULTS method in sub-domain i is defined as,

$$ {}_i\epsilon = {}_iu - {}_cu \tag{16} $$

where ${}_iu$ and ${}_cu$ are the solutions obtained in the sub-domain i using LESAULTS method and the solution obtained using conventional solver respectively. This error is analysed in the spectral space using Global Spectral Analysis as described in the following sections.

5.1. GSA of LESAULTS method applied to linear convection equation

Consider the linear convection equation (LCE) in independent variables x and t and with a constant phase speed c defined as,

$$ \frac{\partial u}{\partial t} + c\frac{\partial u}{\partial x} = 0, \tag{17} $$

-in the spatial domain $0 \leq x \leq L$. When using the conventional solver, the governing LCE is solved in the domain D shown in Fig. 9. Domain D is discretised using elements of length h. Let the time step chosen while solving the LCE in D be ${}_c\Delta t$ and the corresponding CFL number be ${}_cN_c = c\ {}_c\Delta t/h$.

When using the LESAULTS method, the same governing PDE solved in a two sub-domain configuration is shown in the same Figure. Here the domain D used in the conventional method is divided into two overlapping sub-domains D1 and D2. Similar to the discussion in the previous section, the overlapped zone between D1 and D2 is also shown in the Figure. For the sake of analysis, the same uniform mesh size h is used for discretising domain D1 and D2 including the overlapped zone. To demonstrate the error analysis of LESAULTS method, let the time step used in D1 be the same as that used in the conventional solver, *i.e.* ${}_1\Delta t = {}_c\Delta t$. Similarly, let the time step used in D2 be ${}_2\Delta t = R_{\delta t,1}\,{}_1\Delta t = R_{\delta t}\,{}_c\Delta t$. Let the

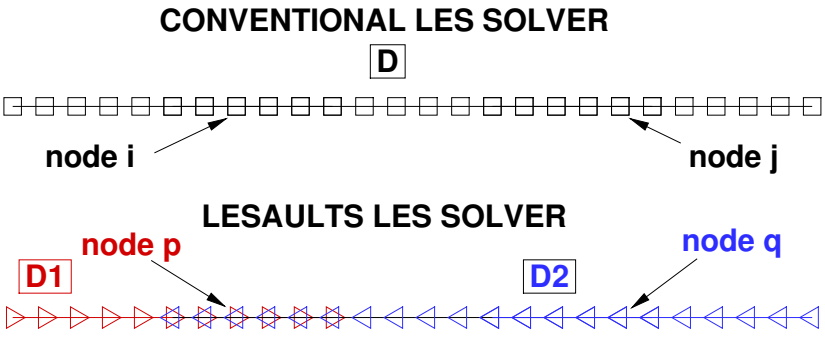

Fig. 9: 1D domains used to solve 1D LCE using conventional and LESAULTS methods

corresponding CFL numbers be denoted by ${}_1N_c$ and ${}_2N_c$ respectively where ${}_2N_c = R_{\delta t,1}\,{}_1N_c = R_{\delta t}\,{}_cN_c$. Hence, for this configuration under study, D1 undergoes $R_{\delta t}(= R_{\delta t,1})$ intermediate time integration steps while D2 undergoes 1 time integration step before the solution synchronization stage.

The numerical solution at the node number i in Domain D (shown in Fig. 9) and at time t^n is expressed using its Fourier transform as,

$$ {}_cu_i{}^n = \int {}_c\hat{U}(k,t^n)\, e^{i\,k\,x_i}\, dk, \tag{18} $$

The numerical solution at time level t^{n+1} (after $R_{\delta t}$ time steps) is given by,

$$ {}_cu_i{}^{n+1} = \int G_{int}^{R_{\delta t}}(kh, {}_cN_c)\, {}_c\hat{U}(k,t^n)\, e^{i\,k\,x_i}\, dk, \tag{19} $$

where $G_{int}^{R_{\delta t}}(kh, {}_cN_c)$ is the net amplification factor after $R_{\delta t}$ time steps.

Similarly, the solution at a coincident node (node p in Fig. 9) in sub-domain D1 at time level t^{n+1} is given by,

$$ {}_1u_p{}^{n+1} = \int G_{int}^{R_{\delta t}}(kh, {}_1N_c)\, {}_1\hat{U}(k,t^n)\, e^{i\,k\,x_p}\, dk, \tag{20} $$

Here, it is evident that node p is located upstream of the node at which the Heaviside-like function is anchored and hence the error from the boundary condition is not present at this node. The amplification factor value used in the above expressions is that of the interior nodes provided in Appendix A.

Since sub-domain D2 undergoes only 1 intermediate time integration step, the solution at any node q in D2 is given by,

$$ {}_2u_q{}^{n+1} = \int G_{int}(kh, {}_2N_c)\, {}_2\hat{U}(k,t^n)\, e^{i\,k\,x_q}\, dk, \tag{21} $$

Similarly, at the corresponding node j in Domain D, the solution is expressed as,

$$ {}_cu_j{}^{n+1} = \int G_{int}^{R_{\delta t}}(kh, {}_cN_c)\, {}_c\hat{U}(k,t^n)\, e^{i\,k\,x_j}\, dk, \tag{22} $$

By definition, the error at node p in sub-domain D1 is given by,

$$\epsilon_p = {}_1u_p{}^{n+1} - {}_cu_i{}^{n+1}, \tag{23}$$

Substituting Eqs. 20 and 19 in 23 one obtains,

$$\epsilon_p = \int \left[G_{int}^{R_{\delta t}}(kh, {}_1N_c) - G_{int}^{R_{\delta t}}(kh, {}_cN_c) \right] \hat{U}(k, t^n)\, e^{i\,k\,x_i}\, dk \tag{24}$$

It is assumed that ${}_c\hat{U}(k,t^n) = {}_1\hat{U}(k,t^n) = {}_2\hat{U}(k,t^n) = \hat{U}(k,t^n)$ since the initial solution is the same in all domains.

Since ${}_1N_c = {}_cN_c$, the error ϵ_p is identically zero. This expression is valid for all nodes in D1 except those at which the Heaviside-like function is non-zero.

Similarly the error at the node q in D2 is given by,

$$\epsilon_q = \int \left[G_{int}(kh, {}_2N_c) - G_{int}^{R_{\delta t}}(kh, {}_cN_c) \right] \hat{U}(k, t^n)\, e^{i\,k\,x_q}\, dk \tag{25}$$

It is to be noted that ϵ_q is not equal to zero since the CFL numbers in sub-domain D2 and domain D are different. The magnitude of the first term in the above integral is a measure of the dissipative error and is given by,

$$\epsilon_G = |G_{int}(kh, {}_2N_c) - G_{int}^{R_{\delta t}}(kh, {}_cN_c)| \tag{26}$$

The non-dimensional error in phase speed and the group velocity are then given by,

$$\epsilon_{CN} = \frac{({}_2C_{num}{}^{n+1} - {}_cC_{num}{}^{n+1})}{c} \tag{27}$$

$$\epsilon_{Vgn} = \frac{({}_2V_{g,num}{}^{n+1} - {}_cV_{g,num}{}^{n+1})}{c} \tag{28}$$

where ${}_2C_{num}$ and ${}_cC_{num}$ are the phase speeds and ${}_2V_{g,num}$ and ${}_cV_{g,num}$ are the group velocities and are functions of the kh and N_c for any numerical scheme. These expressions have been derived and are provided in Appendix.

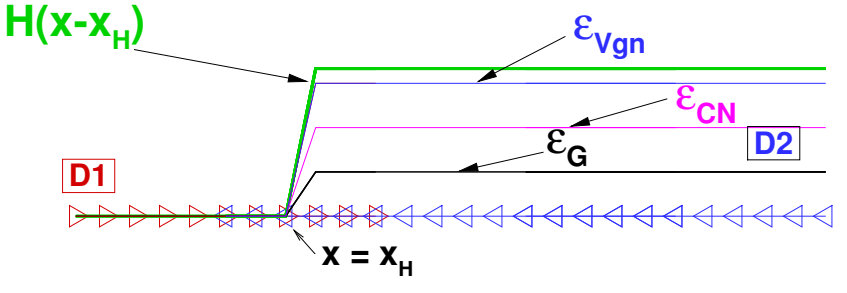

Fig. 10: A schematic showing the Heaviside-like function and the various errors incurred in LESAULTS configuration

Fig. 10 shows a schematic of the spatial variation of error $\epsilon_G, \epsilon_{Vgn}$ along the sub-domains D1 and D2. The Heaviside-like function is also shown in the Figure. The above analysis shows that the error in sub-domain D1 is zero for all nodes upstream of $x = x_H$. The errors in D2 on the other hand, are provided by expressions 26 and 28.

5.2. Error due to LW and TTGC schemes

The above expressions for dissipative, phase speed and dispersive errors are now calculated using Eqs. 26 to 28 for $R_{\delta t}$ values of 2,5 and 10 for the LW and TTGC schemes.

The plots of ϵ_G in the $kh - N_c$ plane for LW and TTGC schemes are shown in Fig. 11. In the Figure, N_c refers to the largest value of CFL used in either of the sub-domains. The region where the dissipative error ϵ_G is less than 1% is colored in grey. It can be observed that for LW scheme with $R_{\delta t} = 2$, LESAULTS scheme is able to resolve the solution amplitude within 1% error for all spatial frequencies up to a N_c value of 0.1. The corresponding value of N_c for TTGC scheme for the same value of $R_{\delta t} = 2$ is 0.25. Similarly, LW scheme performs accurately for all values of N_c used for spatial frequencies $kh < 0.5$. The corresponding value for TTGC scheme is $kh = 0.75$. This implies that if one expects high frequency waves (such as in shear layers or contact discontinuities) in overlapped zones, then it is advisable to keep the CFL number in the larger domain less than 0.1 for LW scheme and less than 0.25 for TTGC scheme. If the overlapped zone is devoid of any such high frequency events, then any CFL number can be used. With increasing values of $R_{\delta t}$, the region of dissipation error is observed to shrink gradually as can be observed from the Figure.

The group velocity error obtained with LESAULTS using LW and TTGC scheme is shown in Fig.12. Similar to the plots of ϵ_G, the region with less than 1% error is colored in gray. It is observed that for the LW scheme, the phase speed is captured accurately for all wavenumbers for $N_c < 0.1$ while for the TTGC scheme a higher N_c value ($N_c = 0.2$) could be used for the same error limit of 1%. Similarly, any stable value of N_c could be used to resolve the group velocity of the input signal with a spatial frequency with $kh < 0.2$. TTGC scheme on the other hand, can resolve wavenumbers up to a value of $kh = 0.3$ with any value of N_c. Similar to the observation for ϵ_G, the error region for the group velocity shrinks progressively with increasing values of $R_{\delta t}$.

5.3. Validation of error analysis for LCE

The LCE with unit phase speed c is solved numerically in a domain extending from $x = 0$ to $x = 3$. For applying the LESAULTS method, the domain is divided into three sub-domains-D1, D2 and D3 as shown in Fig.13(a). All three sub-domains are discretised using a constant meshing size, $h = 0.01$. The CFL numbers in the sub-domains D1, D2 and D3 are ${}_1N_c$,${}_2N_c$ and ${}_3N_c$ respectively such that ${}_1N_c = {}_3N_c = 10 \times {}_2N_c$ and $R_{\delta t,1} = R_{\delta t,3} = 1, R_{\delta t,2} = 10$. The size of the overlapped zones is determined using the recommended size as mentioned in Section 4. The initial solution provided is that of a wavepacket given by

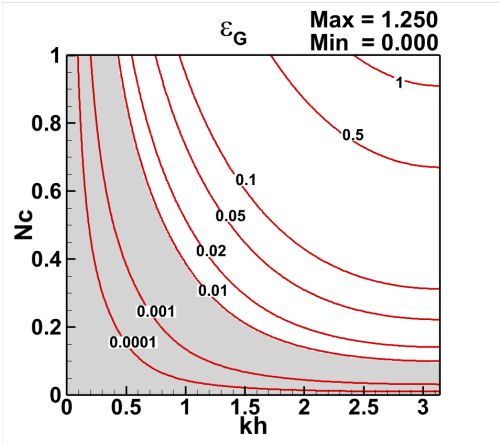

(a) $R_{\delta t} = 2$

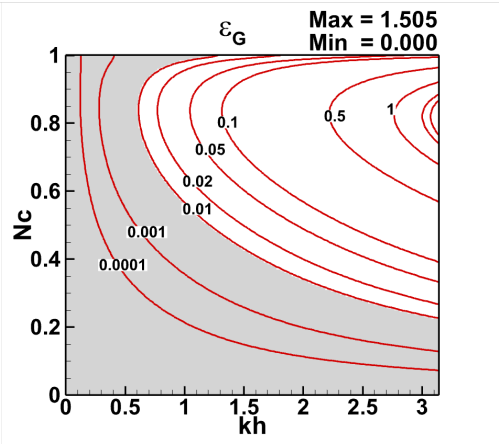

(b) $R_{\delta t} = 2$

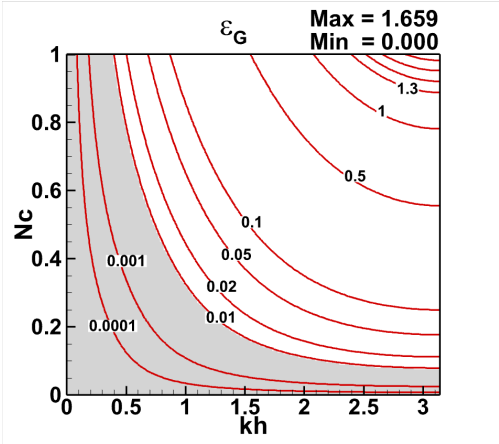

(c) $R_{\delta t} = 5$

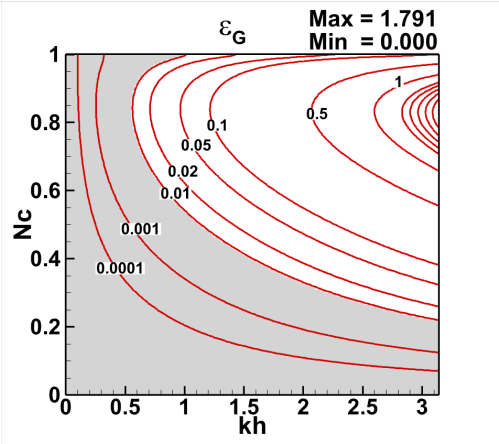

(d) $R_{\delta t} = 5$

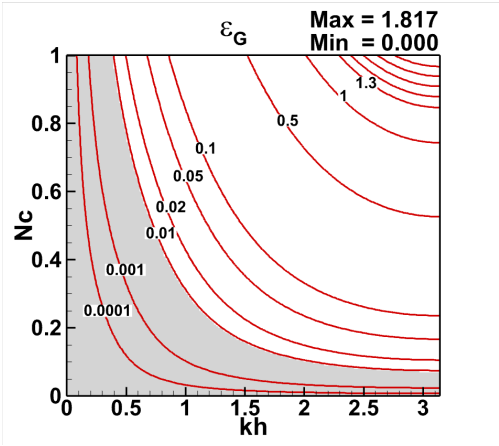

(e) $R_{\delta t} = 10$

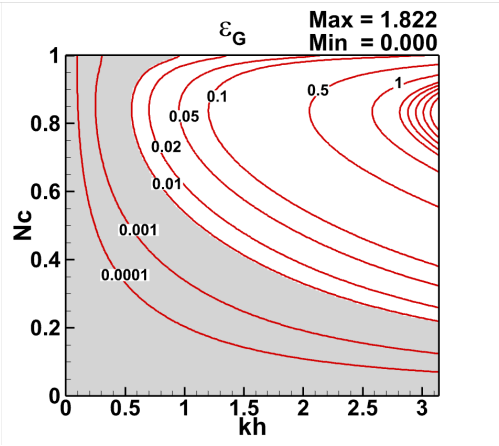

(f) $R_{\delta t} = 10$

Fig. 11: Contours of ϵ_G for LW and TTGC schemes at various values of $R_{\delta t}$

$$u(x,0) = \frac{1}{\sigma\sqrt{2\pi}} e^{\frac{-0.5(x-0.5)^2}{\sigma^2}} \tag{29}$$

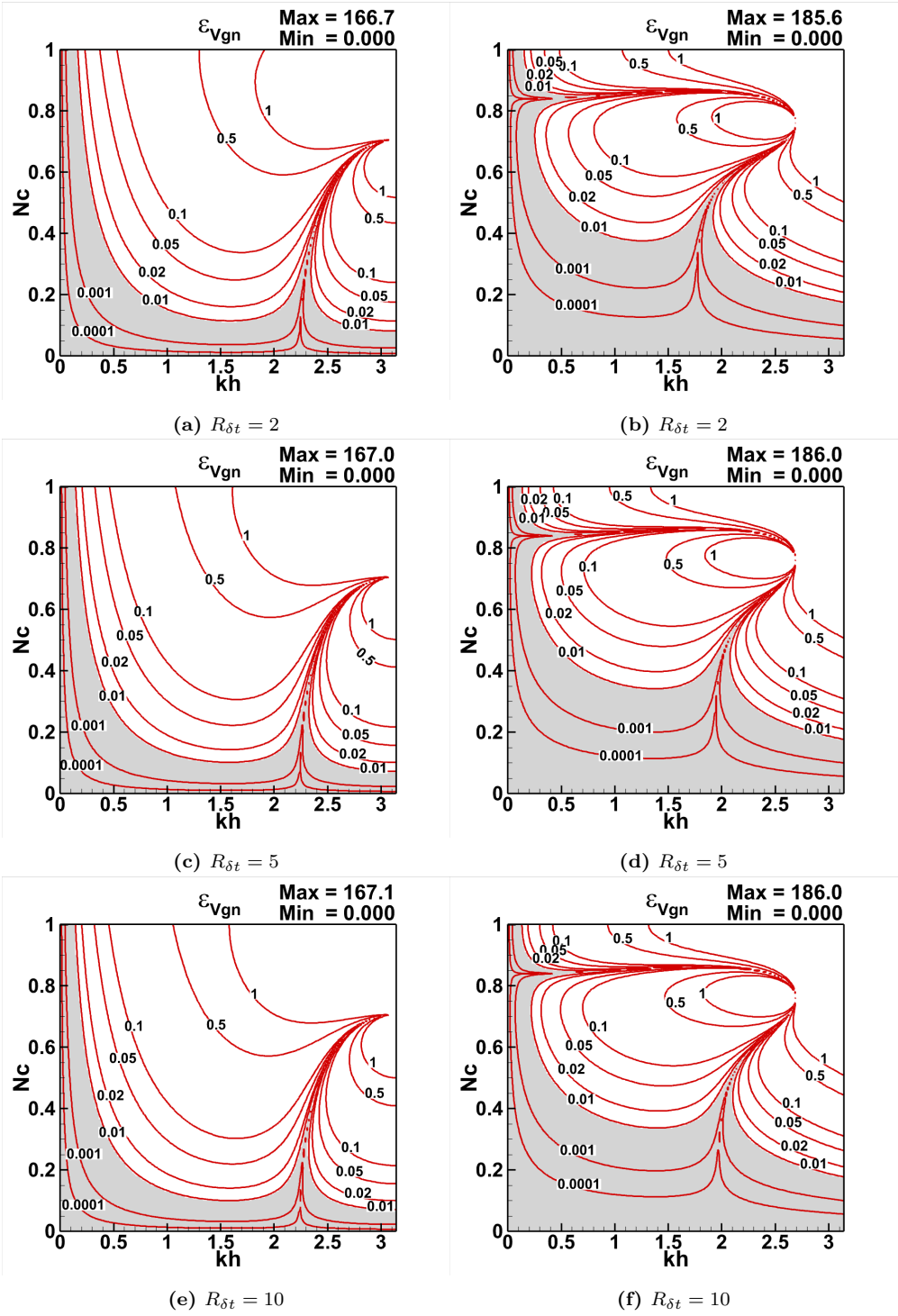

(a) $R_{\delta t} = 2$ (b) $R_{\delta t} = 2$

(c) $R_{\delta t} = 5$ (d) $R_{\delta t} = 5$

(e) $R_{\delta t} = 10$ (f) $R_{\delta t} = 10$

Fig. 12: Contours of ϵ_{Vgn} for LW and TTGC schemes at various values of $R_{\delta t}$

shown in Fig.13(a). The wavepacket is centered at $x = 0.5$ with the non-dimensional central wavenumber $kh = 0.5$. σ is given a value of 0.05.

A total of four numerical tests are carried out, the details of which are provided in Table 2. In all the

tests, the value of $R_{\delta t}$ is fixed as 10. For each numerical scheme, two tests are carried out: one using a high value of ${}_1N_c = {}_3N_c = 0.5$ (tests 1 and 3) and the remaining two tests with a lower value of ${}_1N_c = {}_3N_c = 0.05$ (tests 2 and 4). The values of the dissipation and dispersion errors obtained from GSA explained in the previous section are also provided in the Table.

From Table 2, it is observed that the dissipation error is close to two orders larger for case 1 (with ${}_1N_c = {}_3N_c = 0.5$) when compared to case 2 with ${}_1N_c = {}_3N_c = 0.05$. Hence, it is expected that for the given numerical setup, (kh,N_c and $R_{\delta t}$) case 1 will be prone to more dissipation error than case 2. Similarly when comparing GSA predictions for Cases 1 and 3, it is observed that the error for the LW scheme (case 1) should be higher when compared to TTGC scheme (case 3). It is also observed that the dispersion error ϵ_{Vgn} is reduced by 2 orders of magnitude for the LW scheme when ${}_1N_c = {}_3N_c$ is reduced from 0.5 to 0.05. For the TTGC scheme, dispersion error is reduced by 4 orders of magnitude.

Case No	Scheme	$N_{c,1} = N_{c,3}$	$N_{c,2}$	ϵ_G	ϵ_{Vgn}
1	LW	0.50	0.050	2.9×10^{-3}	3.28×10^{-2}
2	LW	0.05	0.005	1.7×10^{-5}	3.35×10^{-4}
3	TTGC	0.50	0.050	8.1×10^{-4}	1.45×10^{-2}
4	TTGC	0.05	0.005	2.8×10^{-8}	9.37×10^{-7}

Table 2: Numerical tests performed using LESAULTS method for the LCE. ϵ_G and ϵ_{Vgn} values provided are from GSA

All tests (1-4) are computed till time $t = 2$ and the results are plotted in Fig.13. The dashed lines denote the conventional solver solution while the black lines are the solutions obtained using LESAULTS method. The solutions from Cases 1 and 2 using the LW scheme show both the damping and distortion of the initial solution even for the conventional method. The dispersive nature of the LW scheme is well-studied and reported. When comparing the solutions obtained using LW scheme (Cases 1 and 2), Case 1 shows a fair amount of differences between the computed solutions using conventional and LESAULTS method when compared to Case 2. This is in line with the predictions from GSA shown in Table 2 where a higher dissipation error is predicted for Case 1. On the other hand, in the case of TTGC scheme, the amplitude and shape of the initial wavepacket are well preserved highlighting the superior DRP properties of TTGC scheme. When comparing the solutions obtained using LESAULTS method (Cases 3 and 4), it is observed that the solutions are in good agreement with each other even for the high N_c test case (Case 3). When comparing the error between LW and TTGC schemes for the higher N_c tests, it is observed that TTGC scheme incurs lesser error with LESAULTS method. This is also in line with GSA predictions, dissipation error of TTGC scheme is half that of the LW scheme. For the lower N_c case with TTGC scheme (Case 4), the match between the solutions is excellent. This set of tests ascertain the validity of GSA as well as the accuracy of LESAULTS method at lower N_c values.

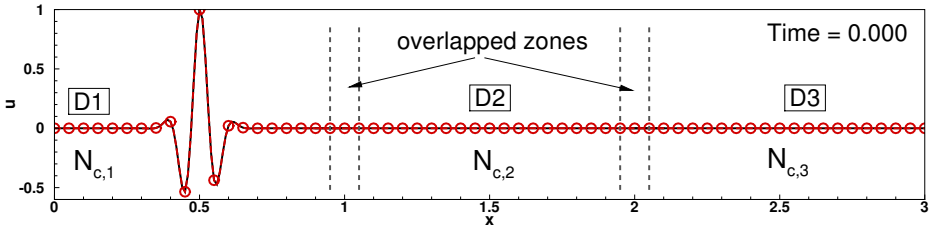

(a) LESAULTS configuration and initial solution

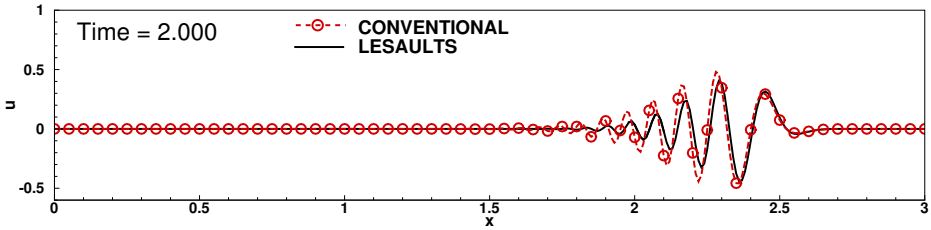

(b) LW, ${}_1N_c = N_{c,3} = 10\ N_{c,2} = 0.5$

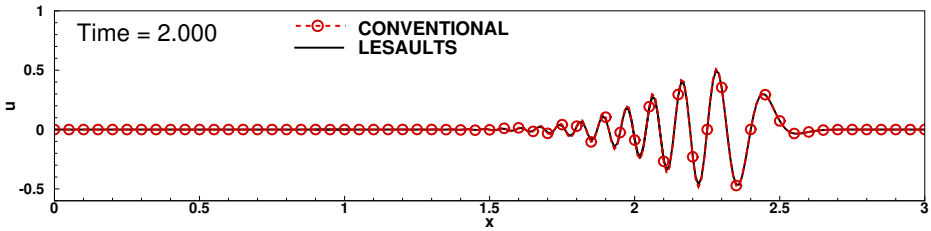

(c) LW, $N_{c,1} = N_{c,3} = 10\ N_{c,2} = 0.05$

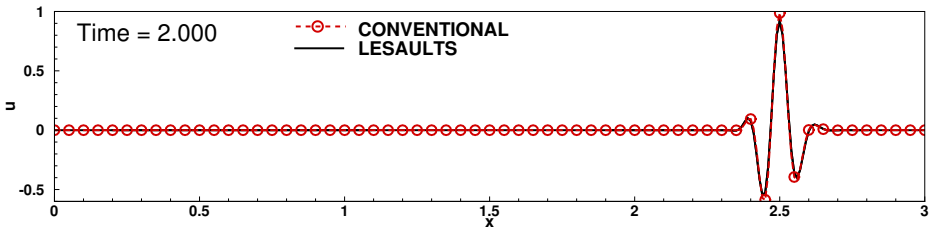

(d) TTGC, $N_{c,1} = N_{c,3} = 10\ N_{c,2} = 0.5$

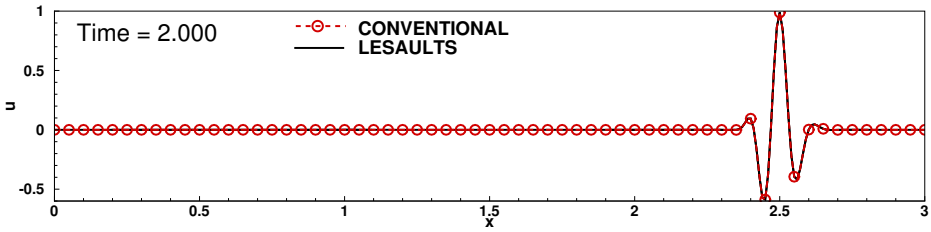

(e) TTGC, $N_{c,1} = N_{c,3} = 10\ N_{c,2} = 0.05$

Fig. 13: LESAULTS method applied to the solution of LCE. The initial solution is provided as a wavepacket centered at $x = 0.5$ and $kh = 0.5$. Straight lines indicate LESAULTS solution and dashed lines indicate conventional solution

5.4. Order of accuracy

To prove that the order of accuracy of the numerical scheme is preserved in LESAULTS method, numerical tests using LCE as the governing PDE are performed. The spatial domain for the numerical tests is kept

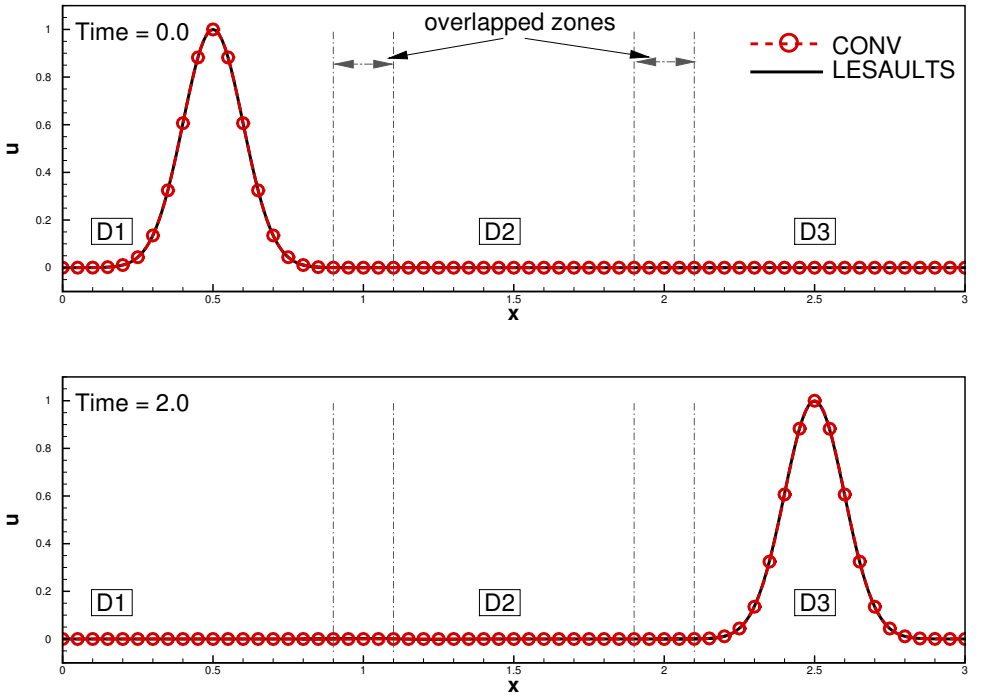

Fig. 14: LESAULTS approach used to solve the test case with initial solution of Gaussian curve

the same as that in the previous section. In the present test cases, the grid sizes are varied. Tests are performed using conventional and LESAULTS method, for both LW and TTGC schemes and with grid spacing $h = 0.1, 0.01, 0.001$ and 0.0001. The CFL number in domains D1 and D3 are kept as 0.1 ($N_{c,1} = N_{c,3} = 0.1$) and the value of $R_{\delta t,2}$ is set as 10 ($N_{c,2} = 0.01$) in all the test cases. The initial solution is provided in the form of a Gaussian curve centered at $x = 0.5$. All the tests are performed till time $t = 2$ is reached.

The conventional and LESAULTS solutions at the initial and final times computed using TTGC scheme with a mesh size of 0.01 is shown in Fig. 14. Since the objective is to assess the order of accuracy using LESAULTS method, a metric for error $Error_{\text{inf}}$ is defined as follows,

$$Error_{\text{inf}} = \frac{max(u - u_{exact})}{max(u_{exact})} \tag{30}$$

-where u and u_{exact} are the computed and exact solutions of LCE for the given initial solution respectively. This error norm is evaluated at the last iteration.

The computed error norm $Error_{\text{inf}}$ for various grid sizes is shown in Fig. 15(a) for the LW scheme and in Fig. 15(b) for the TTGC scheme. It is observed that the error obtained using LESAULTS method is in very close proximity to that obtained using the conventional solver. This is in line with the GSA analysis and its numerical validation presented in the previous section. The order of accuracy as shown by the slope of the curve demonstrates that the second-order spatial accuracy of LW and third-order spatial accuracy of TTGC

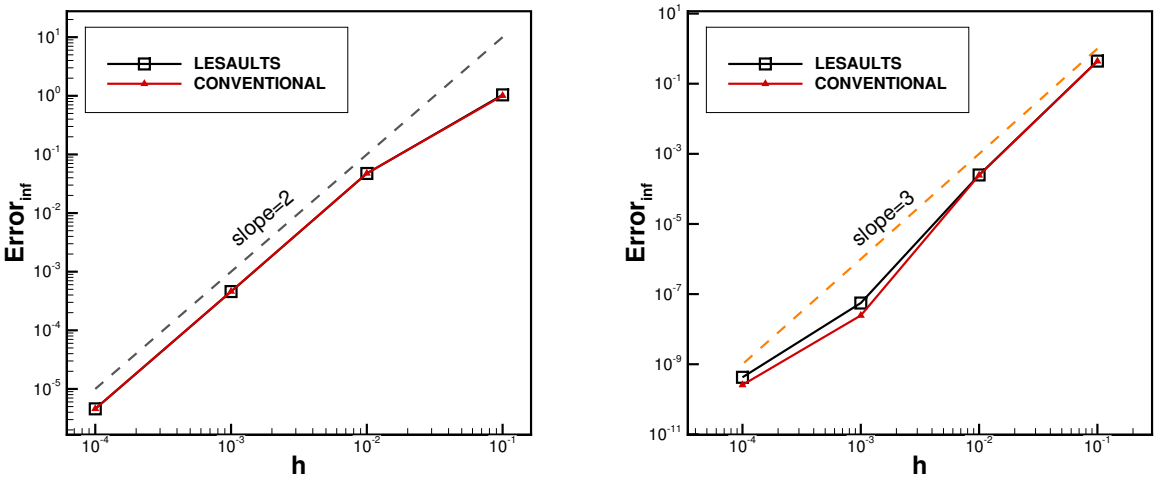

(a) LW **(b)** TTGC

Fig. 15: Error calculated for various mesh size h using LW and TTGC schemes for Rdt=10

is exactly reproduced using LESAULTS method as well. Hence, through these numerical experiments, it is demonstrated that the order of the schemes are well preserved when LESAULTS method is used.

5.5. Conservation property of LESAULTS method

Due to its inherent design, LESAULTS method is not strictly conservative in nature. In order to study the conservation properties of LESAULTS method, a two sub-domain LESAULTS configuration is used to solve LCE and the corresponding conventional solver configuration as shown in Fig. 16. The CFL number used in the domains D and D1 (${}_cN_c$ and ${}_1N_c$) are equal while the CFL number in D2 is large (${}_2N_c = R_{\delta t}\ {}_cN_c$). The overlapped zone in the LESAULTS configuration is shown as ω_L and the similar region in the conventional solver domain is denoted as ω_C in the Figure.

Integrating the LCE (given by Equation 17) in space in the domain ω_c and after numerically evaluating the flux residual at the cell faces one obtains,

$$\frac{d}{dt}\int_{\omega_c} u d\omega = c\left[{}_cu_i - {}_cu_j\right] \tag{31}$$

Similarly, when the same integration is performed for the LESAULTS configuration over the overlapped region ω_L the following expression is obtained,

$$\frac{d}{dt}\int_{\omega_L} u d\omega = c\left[{}_2u_1 - {}_1u_{N_1}\right] \tag{32}$$

Subtracting Equation 31 from 32 one obtains,

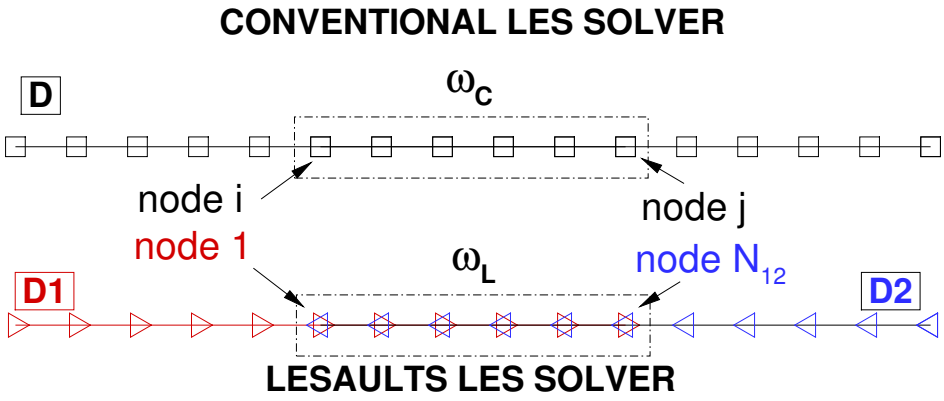

Fig. 16: The computational domain used in a conventional and two sub-domain LESAULTS method. ω_L denote overlapped zones in the LESAULTS configurartion and ω_C denotes the corresponding nodes in the conventional domain

$$\frac{d}{dt}\int_{\omega_L} u d\omega - \frac{d}{dt}\int_{\omega_c} u d\omega = c\left({}_2u_1 - {}_cu_i\right) - \left({}_1u_{N_1} - {}_cu_j\right) \tag{33}$$

Since the conventional solver is assumed to be conservative in nature, the second integral in Eq. 33 drops to zero under steady state conditions. Since ${}_cN_c = {}_1N_c$ and the grid sizes in domain D and D1 are equal, it is proven in Section 5.1 that ${}_2u_1 = {}_cu_i$. Hence the error in conservation is given by $({}_2u_{N1} - {}_cu_j)$. Applying spectral analysis one can observe that this term is exactly the same as the dissipation error ϵ_G derived in Section 5.1 when analysed in the spectral space. Hence the discussions on the dissipation errors provided in Section 5.1 holds valid for the error in conservation as well. It has been concluded in the analysis on dissipation errors earlier, that the dissipation error is minimal for low values of kh and N_c. Hence, the error in conservation is minimum when computations are carried out for low values of N_c and in locations where small values of kh are observed.

6. Numerical Validation

Till now, LESAULTS method is demonstrated to solve LCE on one-dimensional domains with uniform grid spacing. LESAULTS method is now applied to 2-D and 3-D Euler and Navier-Stokes equations using the CFD solver AVBP and are discussed in this section. AVBP is a three-dimensional, hybrid finite-volume/finite-element solver that works on unstructured grids [45]. The purpose of these tests is to study the effect of non-uniform grid topology, cell element types and time step ratio on the performance of LESAULTS method. The 2-D isentropic vortex convection problem is the first among the numerical experiments. This 2-D test case is chosen to study the effect of cell topology as well as the effect of uniform and non-uniform meshes on LESAULTS method. Simulations are carried out using both quadrilateral and triangular elements for values of $R_{\delta t} = 2, 5, 10$. The effect of varying mesh is also analysed by using spatially uniform and varying cells in the domain. The second numerical experiment is the incompressible flow past a 3D cylinder. This test

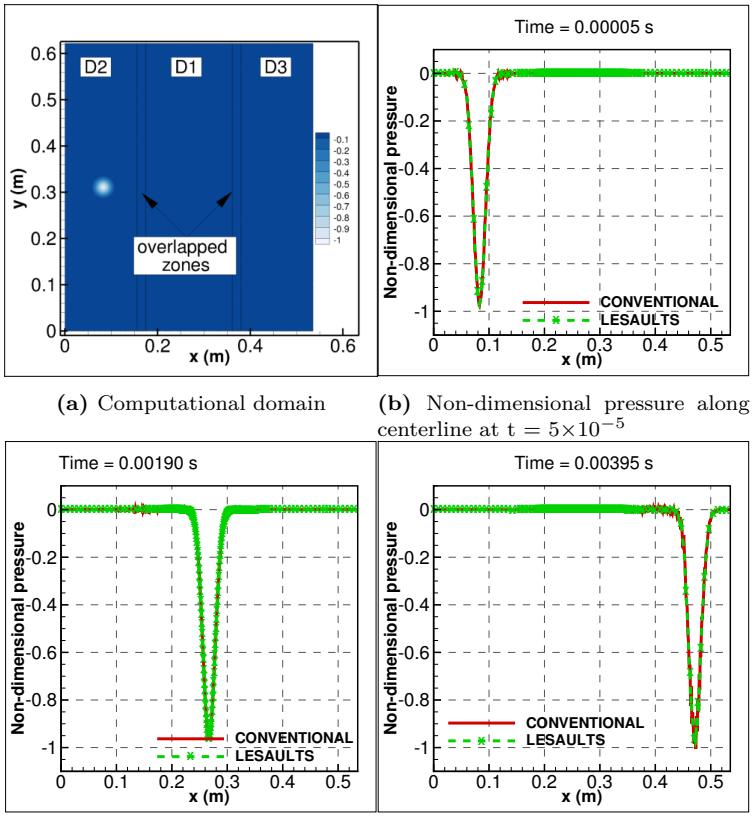

(a) Computational domain

(b) Non-dimensional pressure along centerline at t = 5×10^{-5}

(c) Non-dimensional pressure along centerline at t = 1.90×10^{-3}

(d) Non-dimensional pressure along centerline at t = 3.95×10^{-3}

Fig. 17: (a) Computational domain used in 2d vortex test case, (b,c,d) Non-dimensional pressure along the centerline at various time instants. Solution shown is that of Case 8 of Table. 3

case is chosen to demonstrate the applicability of LESAULTS method for 3-D, transitional flow problems. Hexahedral elements are used in this experiment and the value of $R_{\delta t}$ used is 5. The third and final numerical experiment is performed using the Sandia-D flame. This test case demonstrates the applicability of LESAULTS method for reactive-turbulent flows. Tetrahedral elements are used in this experiment with the value of $R_{\delta t}$ chosen as 4. Through the above mentioned three numerical experiments, the applicability of LESAULTS method for a wide class of flow problems with different numerical settings is demonstrated.

6.1. 2-dimensional isentropic vortex convection

In this test case, an isentropic vortex is superposed on uniform flow of an inviscid fluid. This test case is commonly used to validate numerical methods for capturing the right convection speed and amplitude of the vortex. For the present study, a rectangular domain with length approximately 1.4 m and height 0.6224 m is chosen. An isentropic, Rankine vortex of strength 0.01556 units and radius 0.1 m centered at $(x = 0.0778m, y = 0.3112m)$ is superimposed on a uniform flow with velocity of 100 m/s. The top and bottom boundary conditions are made translationally periodic. The left face is provided a characteristic inlet boundary condition and the right face is given a characteristic outflow boundary condition.

Simulations are performed using both conventional and LESAULTS methods. For the conventional solver, a single domain of dimension (1.4×0.6224) is used. For the LESAULTS method, the computational domain is divided in the longitudinal direction into three over lapping sub-domains as shown in Fig. 17(a). The length of the overlapped zones is determined based on the recommended values in section 4. The sub-domain D1 is time integrated with a smaller time step and the remaining two sub-domains use equal, large time steps. This is designed so as to demonstrate the LESAULTS method's applicability to resolve convection from a higher time step region to a lower time step region and vice-versa.

The objective of this exercise is to study the effect of varying mesh sizes and element types on the LESAULTS method. Hence, multiple test cases are simulated to study the effect of these parameters on the accuracy of LESAULTS method, and are listed in Table 3. The test cases are divided into two groups. The first group consisting of cases (1-4) is performed using uniform grid sizes. This implies that the three sub-domains have the same mesh size and are spatially uniform. Hence, sub-domain D1 is computed using a lower N_c value while D2 and D3 use the same N_c value. The first two test cases in the group, namely cases 1 and 2 are performed using LW scheme with quadrilateral and triangular elements respectively. Similarly, the remaining two cases in this group are carried out using TTGC scheme with quadrilateral and triangular elements.

The second group comprising the remaining four cases (5-8) are carried out using non-uniform meshes. In these cases, larger cells are used in sub-domains D2 and D3, while smaller elements are used in sub-domain D1 thereby ensuring spatially uniform N_c values in all sub-domains. Buffer zones are provided in D1 to ensure the smooth and gradual transition of grid size to D2 and D3. This increases the overall length of full domain depending upon the value of $R_{\delta t}$ used. Similar to the previous group, tests are performed each with different schemes (LW and TTGC) and using different element types (triangular and quadrilateral elements) for different values of $R_{\delta t}$ listed in Table 3. To have a fair comparison of the LESAULTS and conventional methods, the conventional method is carried out with the same time step used in D1 in LESAULTS method. To quantify the error with LESAULTS method, the following definition of error is used.

$$\epsilon_{covo} = max(\frac{p_{LESAULTS} - p_{CONV}}{p_{CONV}}) \tag{34}$$

-where p is the pressure at any point in the domain and ϵ_{covo} is computed as the maximum among all points in the domain and at all computed times. Both sets of simulations (conventional and LESAULTS) are solved using the same number of computational cores with the core distribution in LESAULTS obtained from Eq. 3.

6.1.1. Effect of variable mesh sizes

In the test cases with uniform mesh size (Cases 1-4), all the domains are discretised using elements with a characteristic edge length of $h_0 = 1.556 \times 10^{-3}$ m. The time step used in sub-domains D2 and D3 are 1.0×10^{-6} while lower values (depending on the value of $R_{\delta t}$) is used in sub-domain D1. Hence, in these

Case No	Scheme	$\Delta t_2 = \Delta t_3$	Δt_1	Element Type	Mesh Distribution
1	LW	1.0×10^{-6}	$\Delta t_2/(R_{\delta t} = 2, 5, 10)$	Quadrilateral	Uniform
2	LW	1.0×10^{-6}	$\Delta t_2/(R_{\delta t} = 2, 5, 10)$	Triangle	Uniform
3	TTGC	1.0×10^{-6}	$\Delta t_2/(R_{\delta t} = 2, 5, 10)$	Quadrilateral	Uniform
4	TTGC	1.0×10^{-6}	$\Delta t_2/(R_{\delta t} = 2, 5, 10)$	Triangle	Uniform
5	LW	1.0×10^{-6}	$\Delta t_2/(R_{\delta t} = 2, 5, 10)$	Quadrilateral	Varying
6	LW	1.0×10^{-6}	$\Delta t_2/(R_{\delta t} = 2, 5, 10)$	Triangle	Varying
7	TTGC	1.0×10^{-6}	$\Delta t_2/(R_{\delta t} = 2, 5, 10)$	Quadrilateral	Varying
8	TTGC	1.0×10^{-6}	$\Delta t_2/(R_{\delta t} = 2, 5, 10)$	Triangle	Varying

Table 3: Numerical experiments performed using 2-D isentropic vortex convection test case

tests, N_c values in D1 is smaller than D2 (and D3) by a factor equal to $R_{\delta t}$. In test cases 5-8, the mesh size in D1 is $R_{\delta t}$ times smaller than the ones used in D2 and D3 (h_0). Hence, in these tests the CFL numbers in all three sub-domains are nearly uniform.

Fig. 17(b,c,d) shows the convection of the Rankine vortex simulated using the LESAULTS method (in dashed lines with markers) and the conventional method (in straight lines). Results from the most extreme test (Case 8) with non-uniform triangular mesh and with a time step ratio of 10 are shown. Excellent match is found between the conventional and LESAULTS method solutions in the non-dimensional pressure. It is also observed that the overlapped zones do not create any spurious oscillations as the vortex convects from one sub-domain to the adjacent through the overlapped zone, thanks to the solution synchronization step in the calculations.

The error calculated for both the uniform and varying mesh cases using quadrilateral and triangular elements are shown in Fig. 18(a) and (b). Comparing both the figures, it is concluded that both uniform and varying meshes incur error of the same order of magnitude even though the error for varying meshes is slightly lesser than the uniform ones. As expected, it is also observed that the LW scheme produces more error than the TTGC scheme for both uniform and varying meshes due to its poorer order of accuracy when compared to the TTGC scheme. This is also evident from the GSA analysis and the discussion on the dissipation error ϵ_G that demonstrates a lower error for TTGC when compared to LW for the same value of N_c and kh. Similarly, the error ϵ_{covo} is also found to increase with increasing values of $R_{\delta t}$ for the both uniform and varying meshes.

6.1.2. Effect of mesh element type

Fig. 18 also depicts the error incurred for different mesh elements. Quadrilateral elements are found to incur lower error when compared to triangular meshes for both schemes. This observation is valid for both uniform and varying meshes. It is also observed that error due to TTGC scheme is considerably lower than the ones for LW scheme. This is obvious and underlines the superior numerical property of TTGC scheme. Both the element types exhibit similar variation in error with $R_{\delta t}$, with the error increasing with increasing $R_{\delta t}$.

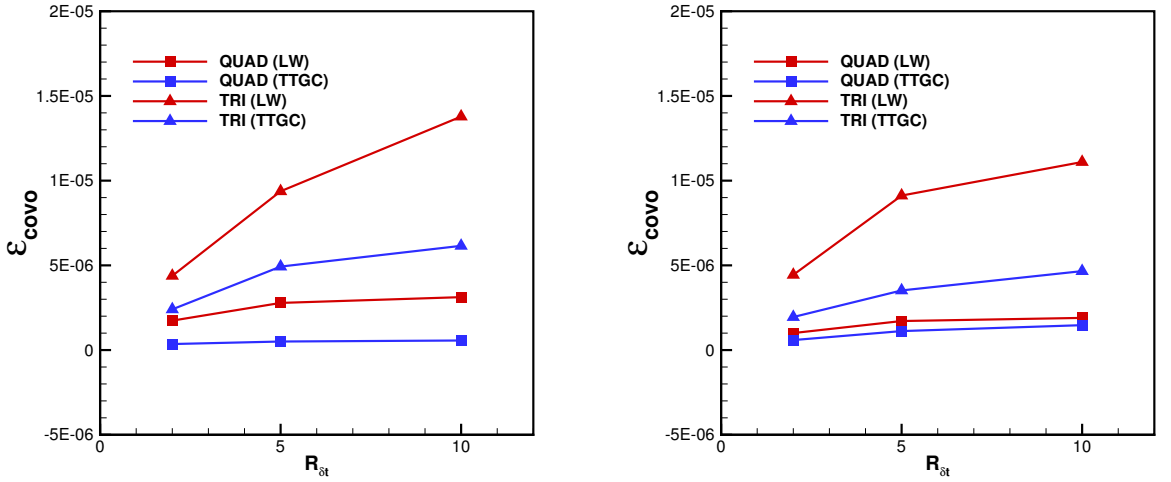

(a) Constant mesh sizing **(b)** Variable mesh sizing

Fig. 18: Error ϵ_{covo} calculated for (a) Uniform mesh spacing (b) Variable mesh spacing

6.1.3. Actual computational speedup

The theoretical and actual speedup obtained during the tests (Cases 1-4) are reported in Table 4. The theoretical speedup is calculated using Eq. 1. In the reported values, the number of nodes in the overlapped zones are not taken into consideration and are hence approximate in nature. The actual speedup S_{act} is obtained by recording the time taken between two successive computations by the solver. The LESAULTS efficiency $\eta_{LESAULTS}$ defined as $\eta_{LESAULTS} = S_{act}/S_{th}$ that gives an indication of how well LESAULTS method works is also provided in the Table. For the sake of brevity, the speedup values are reported only for the extreme case where ($R_{\delta t,1} = 10$) and for uniform grid distribution. Similar speedup values are obtained for the other tests (Cases 5-8).

Case No	Element type	Scheme	$R_{\delta t,1}$	N_1	N_2	N_3	S_{th}	S_{act}	$\eta_{LESAULTS}$
1	Quad	LW	10	50125	40501	40501	2.25	2.21	98%
3	Quad	TTGC	10	58947	40501	40501	2.09	1.92	92%
2	Tri	LW	10	51634	47409	47180	2.39	2.21	92%
4	Tri	TTGC	10	50125	40501	40501	2.31	2.09	90%

Table 4: Theoretical and actual speedup obtained using LESAULTS for tests (1-4)

In all the tests reported in Table 4, actual speedup close to 2 (twice faster) is obtained. This is also close to the theoretical limits set by Eq. 1 ($\eta_{LESAULTS} = 90\%$), thereby emphasizing the benefit of using LESAULTS method over conventional method.

6.2. Flow past 3D circular cylinder

In this section, validation of the LESAULTS method for the 3-dimensional, incompressible, transitional flow past a circular cylinder at Reynolds number 3900 is described. In terms of the nature of turbulence,

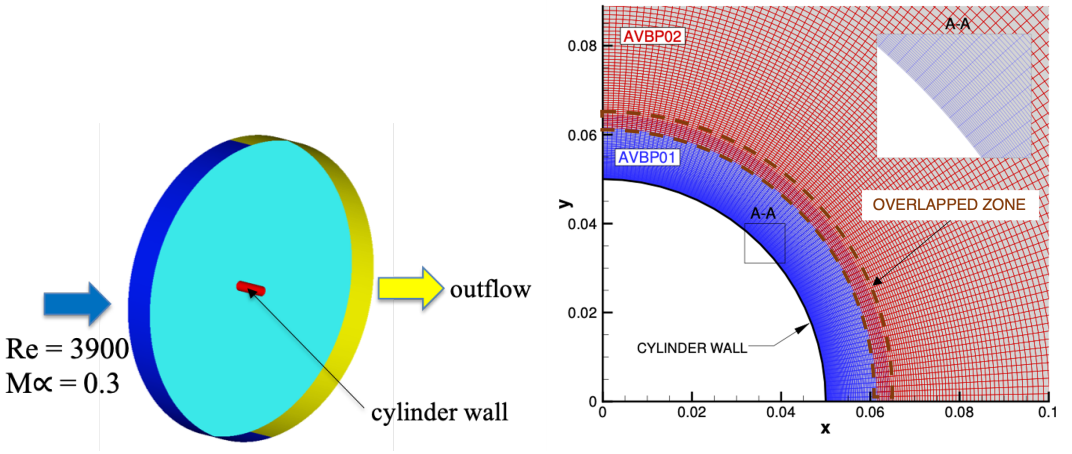

(a) Computational domain and boundary conditions **(b)** Domain decomposition used for LESAULTS method

Fig. 19: Computational domain used to solve the 3D flow past a circular cylinder

this test case falls under the lower subcritical range of flow where the flow is essentially laminar beyond separation and turbulence is generated at the shear layers in the wake. This is a typical test case used to validate DNS ([46, 47]), LES ([48]) and RANS ([49, 50]) solvers with experimental data on the mean and rms values of velocity and pressure available and the details of the measurement technique discussed in [51, 52].

This flow test case is modeled using a circular cylinder of diameter $D = 0.1$ m and a span length equal to π times the diameter ($\pi\ D$) kept laterally facing a uniform incompressible flow of velocity 0.61 m/s. The computational domain used to model the test case is shown in Fig. 19(a). The cylinder is placed in a cylindrical computational domain of diameter $30D$. The upstream semi-cylindrical boundary of the outer domain is modeled as an inlet, while outflow boundary condition is enforced on the downstream side of the cylinder. Similar to the previous test case, NSCBC based inlet and outlet boundary conditions are used in this study. The target pressure at the outflow boundary is specified as atmospheric pressure. The lateral faces of the computational domain are modeled as transitionally periodic to avoid end wall effects. The cylindrical wall is modeled as no-slip and adiabatic and no specific wall treatment is used. Air is used as the fluid for simulation and the viscosity of air is calculated using Sutherland's law. Since the flow is near isothermal, the viscosity is maintained nearly constant. The incoming flow velocity of 0.61 m/s along with the chosen length scale (D) ensures that the Reynold's number for the simulation is 3900.

Two sets of simulations (corresponding to the conventional and LESAULTS solver each) are performed. The mesh is made of hexahedral cells using an 'O-type' grid configuration. It is for this reason that hexahedral grid cells are used since tetrahedral based LES computations of this case would require a huge number of mesh cells considering also the fact that no wall models are used. For properly resolving the fine-scale turbulent structures generated near the cylinder wall, extremely fine cells are used in the near

wall region. The boundary layer thickness on the cylinder at an angle of 80 degrees to the incoming flow is estimated as 0.0476D as mentioned in [53]. The cell size in the wall-normal direction is chosen such that this boundary layer thickness is resolved using 80 cells. The cylindrical wall surface is discretized using 360 elements in the circumferential direction and 40 cells in the span-wise direction respectively. Due to the fine nature of mesh cells near the wall, the time step in the domain is restricted to a very small value. While using the conventional solver, this small time step value induces stiffness and makes the computation exorbitantly high.

For performing the LESAULTS simulation, the computational domain is divided into two sub-domains AVBP01 and AVBP02 as shown in Fig. 19(b). Here AVBP01 is the domain that houses the cylinder wall and consists of 60 cells in the radial direction. This is the sub-domain with the fine cells requiring small time step. AVBP02 consists of the remaining portion of the computational domain and can accommodate a larger timestep.

LES with the conventional explicit solver is also performed for comparing the results of that obtained using LESAULTS method. Here a single computational domain is used, obtained by merging the mesh generated for the LESAULTS method. Hence it is emphasized that the grids used in LESAULTS and conventional simulations have an exact node-to-node spatial correspondence.

Domains	Number of nodes	Time step (s)
Conventional	3704760	2.0×10^{-7}
AVBP01	900360	2.0×10^{-7}
AVBP02	2922480	1.0×10^{-6}

Table 5: Number of nodes and time step used in the 3D cylinder simulations

The simulations are performed using LW scheme for both cases (conventional and LESAULTS) and the Sigma SGS model [54] is used for turbulent closure. For the conventional simulation, a time step of 2.0×10^{-7} sec. is used for the entire sub-domain. For the LESAULTS method, the same time step is used in AVBP01 while a time step of 1.0×10^{-6} sec is used in AVBP02. Hence the value of $R_{\delta t}$ used for this simulation is 5. The number of nodes and the time steps used in the simulations are listed in Table 5. Flow simulations are performed for a duration (in flow time) of 10 secs and averaging is performed over 20 vortex shedding cycles after the flow has reached a statistically steady state. In order to compare the computed values to experimental measurements, a span-wise averaging in addition to time averaging is also performed on the flow quantities.

6.2.1. Actual computational speedup

Both the LES simulations are performed using 720 computing cores on Haswell processors on a Bull B720 machine. The actual and theoretical speedup obtained in the test are listed in Table 6. Using LESAULTS method an actual speed to 2.4 times is obtained for this configuration. This is very close to the theoretical prediction of 2.5 times obtained using Equation 1 giving a LESAULTS efficiency of 92%.

Element type	Scheme	$R_{\delta t,1}$	N_1	N_2	S_{th}	S_{act}	$\eta_{LESAULTS}$
Hexahedral	LW	5	900360	2922480	2.57	2.37	92%

Table 6: Theoretical and actual speedup obtained for the LES of 3D flow past a cylinder

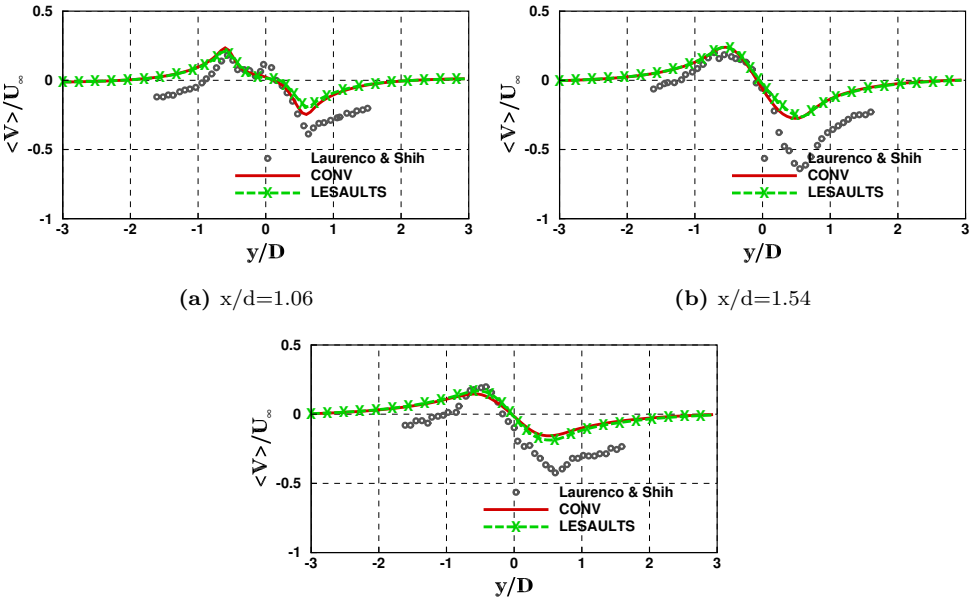

(a) x/d=1.06

(b) x/d=1.54

(c) x/d=2.02

Fig. 20: Variation of non-dimensional mean lateral velocity along non-dimensional y-coordinate at longitudinal planes calculated using conventional and LESAULTS method

6.2.2. Comparison of results obtained using conventional and LESAULTS method

The results obtained using LESAULTS and conventional solvers are presented in Figs. 21 to 24. The lateral variation of the transverse velocity at the midplane is shown in Fig. 20. It is non-dimensionalised using the freestream velocity value and is plotted against the non-dimensional y-coordinate. Discrepancies are observed between the computed and measured values at the near wake planes. However, the computations are able to reproduce the general trends. This observation has been made in previous studies as well [46, 52]. However, excellent match is seen between the conventional and LESAULTS method results underlining the accuracy of LESAULTS method in reproducing the conventional solver results.

The lateral variation of the mean longitudinal components at downstream planes (x/d=1.06,1.54,2.02,4,7 and 10) are plotted in Fig. 21. The PIV measurements of Laurenco and Shih [52] in the near wake region and the hot wire measurements at planes downstream are plotted as symbols. The U-shaped longitudinal mean velocity profile at the near wake ($x/d = 1.06$) plane is shown in Fig. 21(a). At planes downstream, the mean velocity profiles change to a typical V-shape and can be observed for both experimental and computational results. Excellent match between computed (both LESAULTS and conventional) and experimental values are observed in the near wake regions (x/d=1.06,1.54 and 2.02). Further downstream, the element size

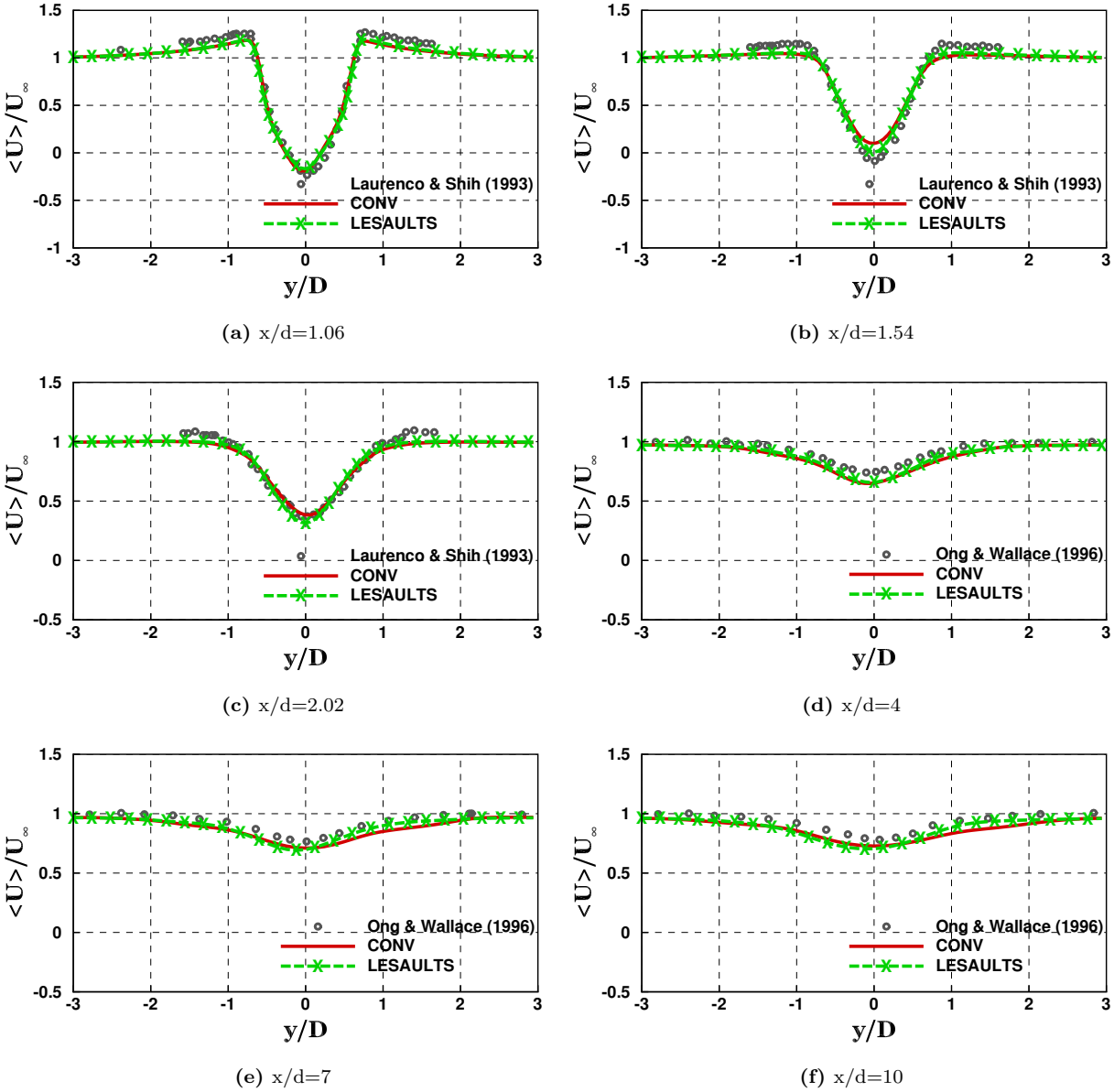

(a) x/d=1.06 **(b)** x/d=1.54

(c) x/d=2.02 **(d)** x/d=4

(e) x/d=7 **(f)** x/d=10

Fig. 21: Variation of non-dimensional mean longitudinal velocity along non-dimensional y-coordinate at longitudinal planes calculated using conventional and LESAULTS method

increases and hence minor differences between the computed and measured values are observed. However, the results from LESAULTS and conventional methods are in good agreement with each other highlighting the accuracy of LESAULTS method.

Similar to the mean quantities discussed previously, the first order turbulent statistical quantities are also plotted in Figs.(22 to 24). The longitudinal component of the resolved turbulent stress non-dimensionalised by freestream velocity as a function of non-dimensional y-coordinate is plotted in Fig. 22. In the near wake region ($x/d < 1.54$), the computed values of the rms of longitudinal velocity are higher than the measured

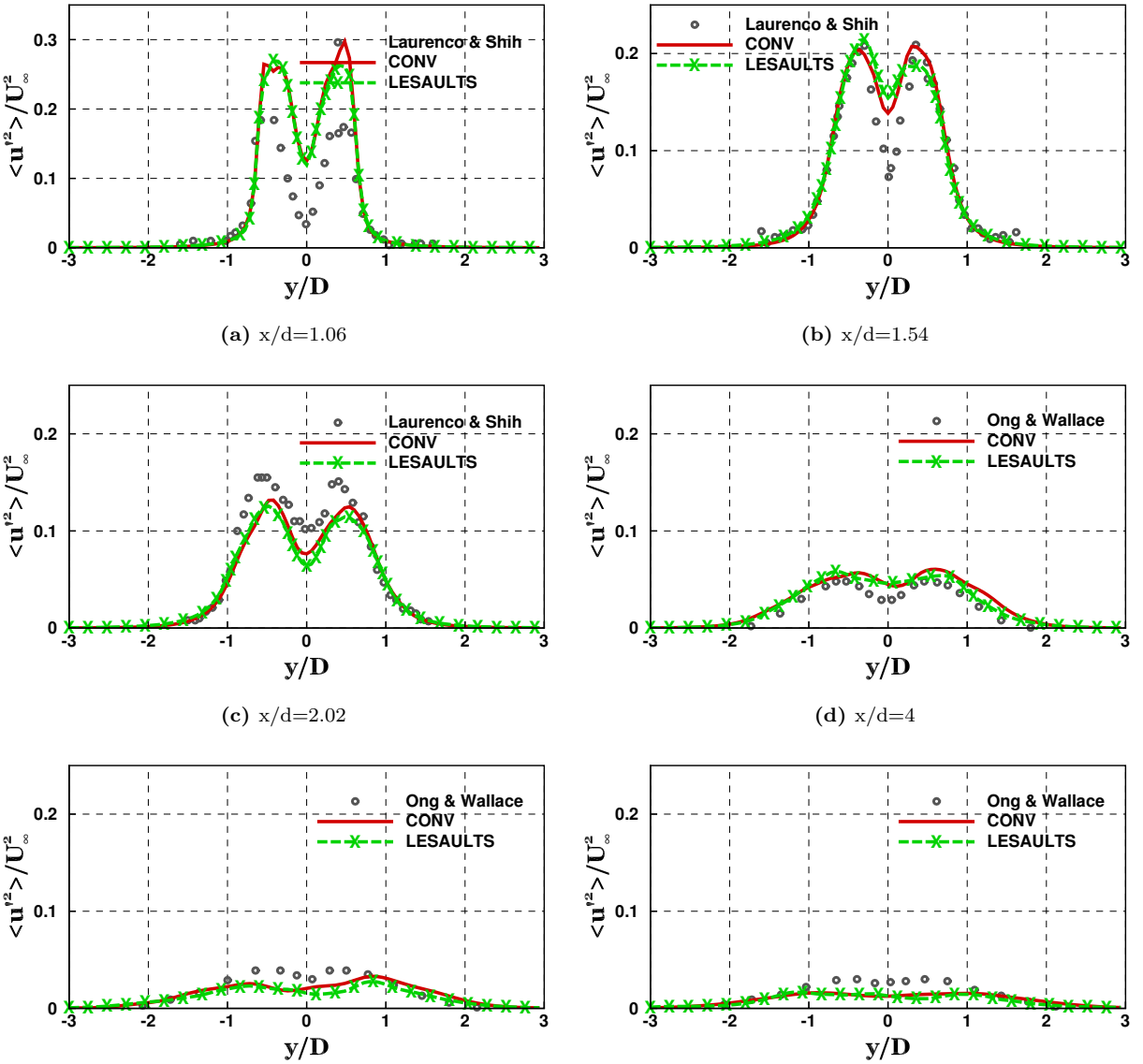

(a) x/d=1.06 **(b)** x/d=1.54

(c) x/d=2.02 **(d)** x/d=4

(e) x/d=7 **(f)** x/d=10

Fig. 22: Variation of non-dimensional U_{rms} along non-dimensional y-coordinate at longitudinal planes calculated using conventional and LESAULTS method

values. At further downstream locations, these values are underpredicted due to relatively coarser meshes there. However, it should be noted that the match between the LESAULTS and conventional method predictions are good.

Similar plots of the lateral component of the resolved turbulent stresses as a function of the non-dimensional distance is shown in Fig. 23. The stress values are overpredicted at the near wake regions ($x/d < 1.54$) whereas a good match is observed between measurements and computations are downstream locations. As observed with the longitudinal stress component, the LESAULTS and conventional results

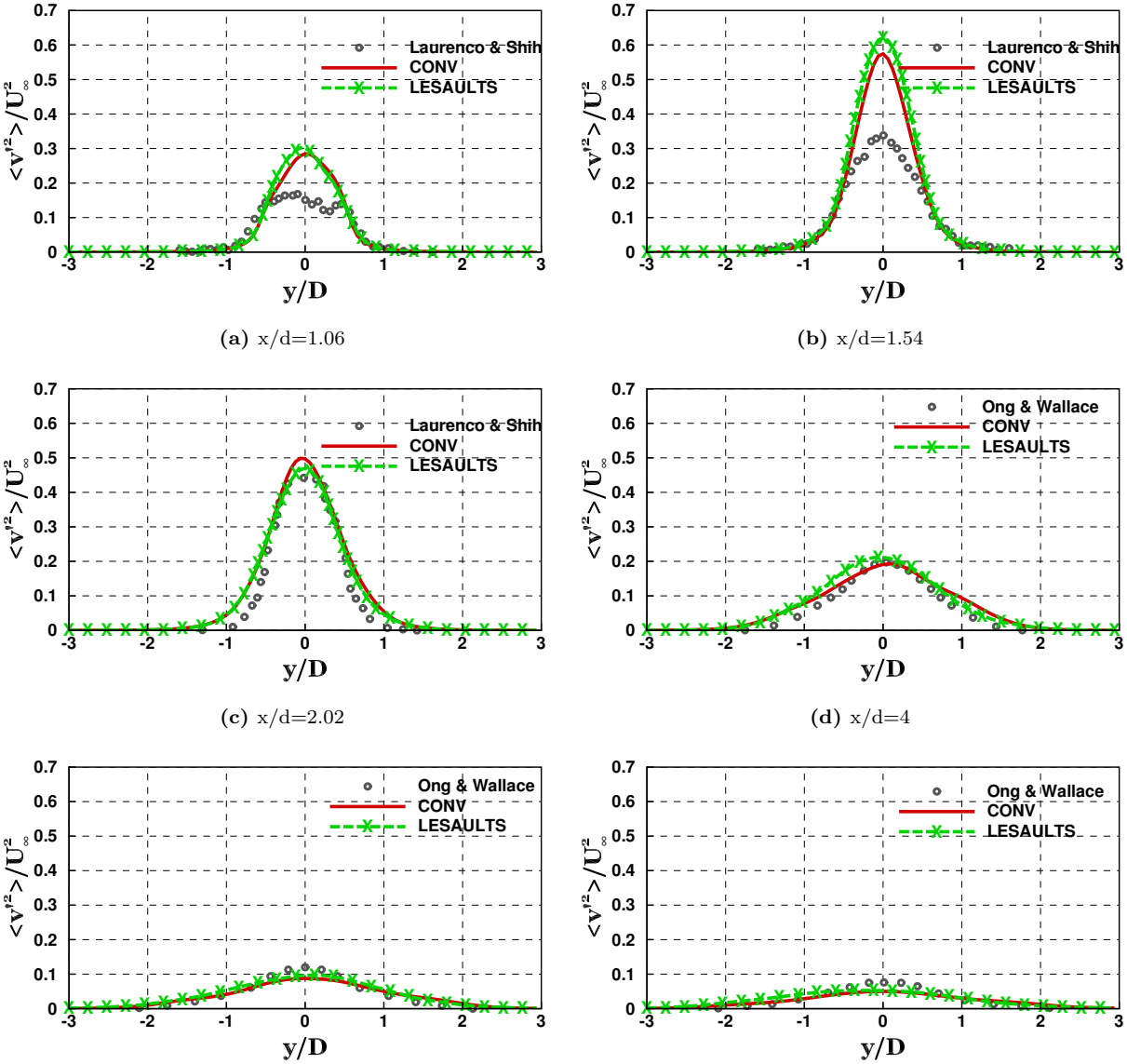

(a) x/d=1.06 **(b)** x/d=1.54

(c) x/d=2.02 **(d)** x/d=4

(e) x/d=7 **(f)** x/d=10

Fig. 23: Variation of non-dimensional V_{rms} along non-dimensional y-coordinate at longitudinal planes calculated using conventional and LESAULTS method

show a very good match with each other.

The resolved cross-stress terms are shown in Fig. 24. Here, a good match is observed between both the computed and measured values as well between LESAULTS and conventional method.

6.3. Sandia-D

The flame D of Sandia is a widely studied partially premixed, turbulent flame with detailed measurements of temperature, mixture fraction and species profiles available. This flame is chosen as a test case to demonstrate the applicability of LESAULTS method to turbulent reactive flow cases. Since hexahedral

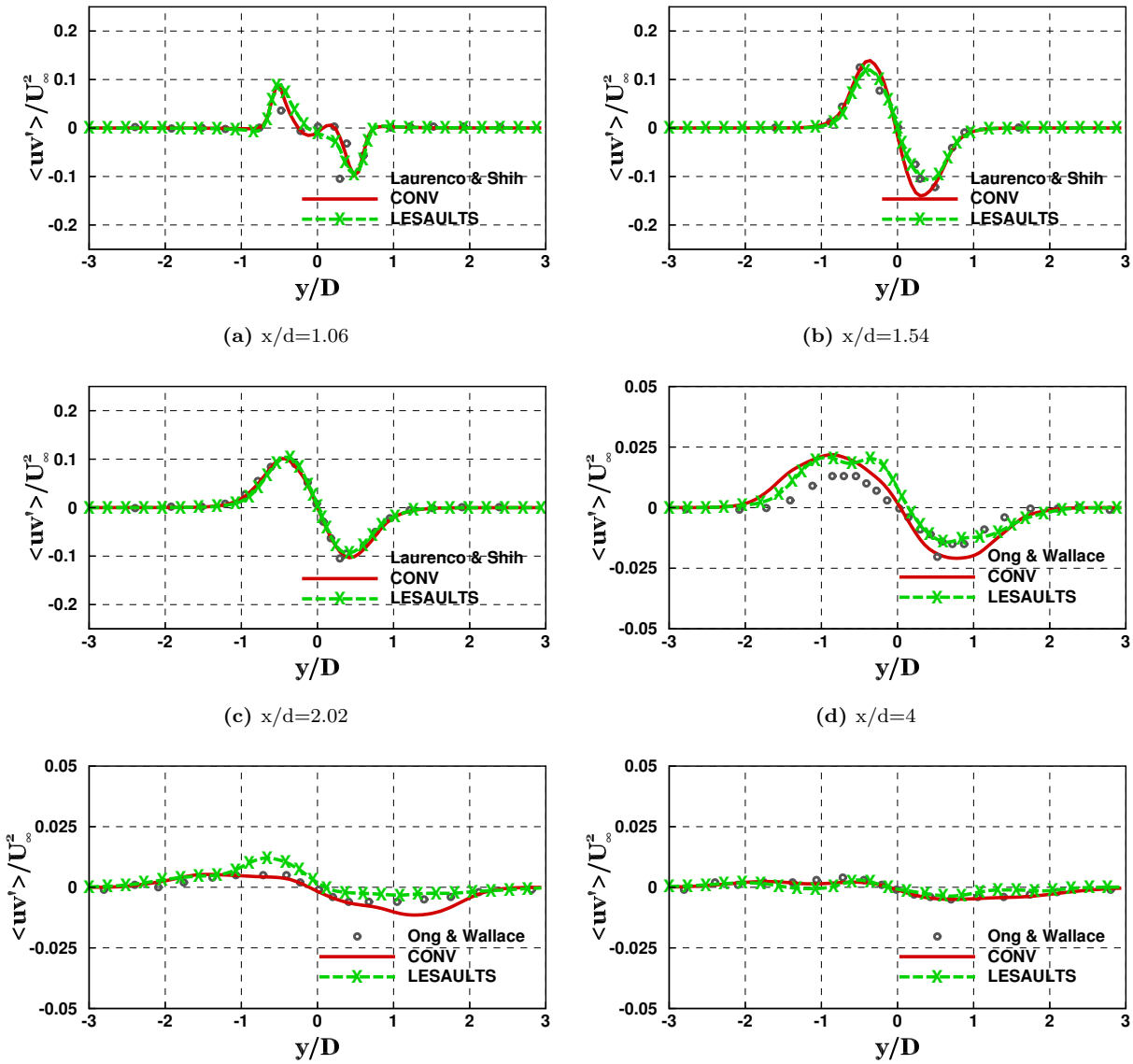

(a) x/d=1.06 **(b)** x/d=1.54

(c) x/d=2.02 **(d)** x/d=4

(e) x/d=7 **(f)** x/d=10

Fig. 24: Variation of non-dimensional UV_{rms} along non-dimensional y-coordinate at longitudinal planes calculated using conventional and LESAULTS method

elements are used in the previous test case, we use tetrahedral cells in this test case.

The domain for studying the flame is shown in Fig. 25. The experimental setup used in the flame consists of a fuel jet emanating out of a cylindrical pipe with an inner diameter of 7.2 mm. The partially premixed fuel consists of 25% methane diluted in air at room temperature. The bulk velocity of the fuel jet is 49.9 m/s. The fuel jet is surrounded by a cylindrical pilot flame produced by the combustion of methane in air at an equivalence ratio of 0.77. The temperature of the burnt gas is measured to be 1880 K. Coflow air at a temperature of 298 K and a bulk velocity 0.9 m/s serves as the oxidizer for sustaining combustion. Available

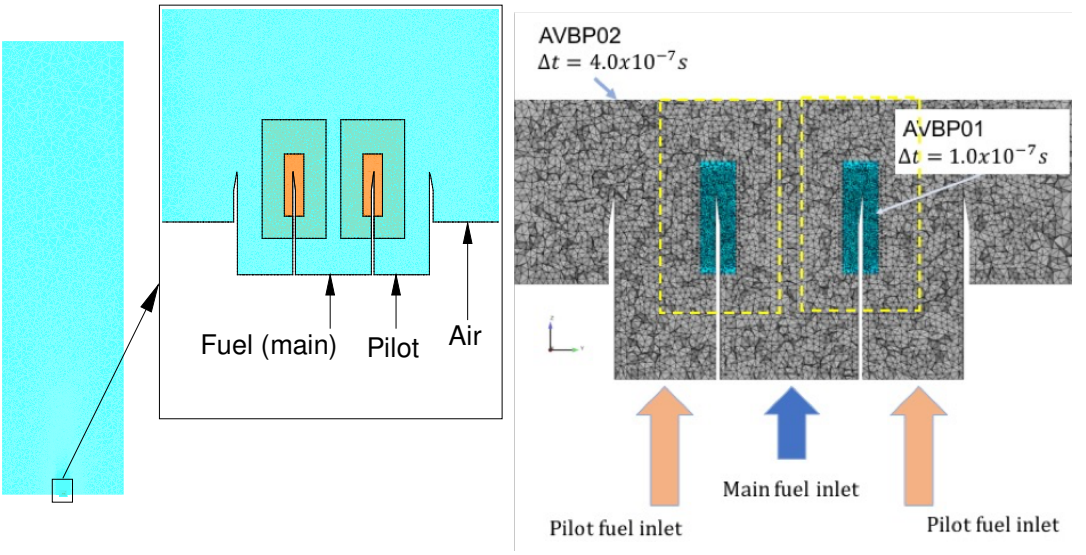

(a) Computational domain used for Sandia-D flame **(b)** Mesh generated for LESAULTS method at the mid-plane

Fig. 25: Computational domain and mesh generated for the Sandia-D flame using LESAULTS method

experimental measurements include mean and rms values of temperature and radial profiles such as major species such as CH_4, O_2, CO_2, CO and NO.

The computational domain used to perform LES of the Sandia-D flame using conventional LES solver is shown in Fig. 25(a). A cylinder of length 1.08 m and diameter of 0.288 m is used as the computational domain. The fuel and the pilot inlet boundaries are provided one diameter upstream of the jet orifice. The long domain length is necessary to capture the flame length and the plume accurately. Tetrahedral grid is generated inside the domain. A fine mesh is used to resolve the regions near the jet exit and the rims. From previous studies ([55]), it is observed that very fine mesh is required near the rim region and in regions upstream to the rims. This is required to ensure that the flame stabilization mechanism is resolved well. Hence very fine cells are used in this region as shown in Fig. 25(b). A cross section of the grid generated is shown in the Figure.

Since it is required to resolve the lip region with very fine cells, the limiting time steps are observed in this region. The large length of the domain (extending to 1.08m) also makes the computations using conventional method costly. Keeping this in mind, for the LESAULTS method, a two sub-domain configuration as shown in Fig. 25(b) is used. The sub-domain AVBP01 comprises of the fine cells where time steps are small. The rest of the domain is included in sub-domain AVBP02. The overlapped zone between AVBP01 and AVBP02 is marked as enclosed by the yellow dotted lines in the Figure.

It is further emphasized that the same grid is used for the LES solution for both the conventional and LESAULTS method solution procedures. This is done by generating the mesh using a multi-zone computational domain in the grid generation software. While the sub-domains are retained for the LESAULTS

method, for the conventional method the multizone grids are merged to form a single grid with an exact node-node spatial correspondence with the LESAULTS grid. The maximum allowable time step that can be used for the conventional LES solution method is 1.0×10^{-7} sec. For the LESAULTS method the same value of time step is used in sub-domain AVBP01. For AVBP02, a time step of 4.0×10^{-7} sec is used ($R_{\delta t} = 4$). Such a knowledge of the typical time step used in conventional LES solver was available from a previous published study ([55]). This indeed allowed the careful choice of defining the geometry of the overlapped zone. It is ensured that the number of cells in the overlapped zone from one interface boundary normal to the other is 6 as mentioned in Section 4.

Since the objective of this exercise is to validate the LESAULTS methodology, a simple 2-step mechanism for methane combustion consisting of 6 species ([56]) is used in this study. Transport properties of this mechanism is based on a unit Le number assumption with the gas mixture viscosity calculated using Sutherlands law. The thermodynamic properties of the mixture is calculated using values from the Jannaf tables. It should be noted that the objective of this particular test case is not to compare with measurement data, but to compare the solutions obtained using LESAULTS and conventional method. As mentioned previously, considering the lower computational cost, LW scheme is used in both the LES computations. The artificial viscosity model of Colin [57] is used to stabilize the computations by damping inadvertent high frequency errors in computations. The SGS model used is that of Sigma. Turbulent Prandtl and Schmidt numbers are fixed as 0.6 respectively.

The boundary conditions are modeled in the following manner. At the fuel inlet, a turbulent velocity profile with the specified volume flow rate, temperature and species mass fractions are specified. Artificial turbulence injection at the fuel inlet is performed with a turbulent intensity of 2%. To model the pilot flame, adiabatic species composition and temperature corresponding to the equivalence ratio of the pilot flame is specified. The axial inlet velocity is specified as 11.4 m/s. Similarly, axial velocity and temperature of air is enforced at the coflow air inlet boundary. At the outlet, a characteristic based outflow boundary is specified with the target outlet pressure fixed to that of the ambient atmosphere.

LES computations using the conventional and LESAULTS method are carried out on high performance computing (HPC) machines comprising Intel E5-2680 processors. 360 computing cores are used for the conventional LES solution while 202 and 158 (total of 360) cores respectively are used for sub-domains AVBP01 and AVBP02 in the LESAULTS method. The core distribution among AVBP01 and AVBP02 is obtained using equation 3 in Section 3. LES computations are performed for a total duration of 8 flow through times (FTT) with time averaging performed for the last 5 FTTs to calculate the mean and rms values.

6.3.1. Actual computational speedup

The actual and theoretical computational speedup obtained for this test case is summarized in Table 7. A speedup of approximately two times is obtained for this test case with the LESAULTS efficiency being

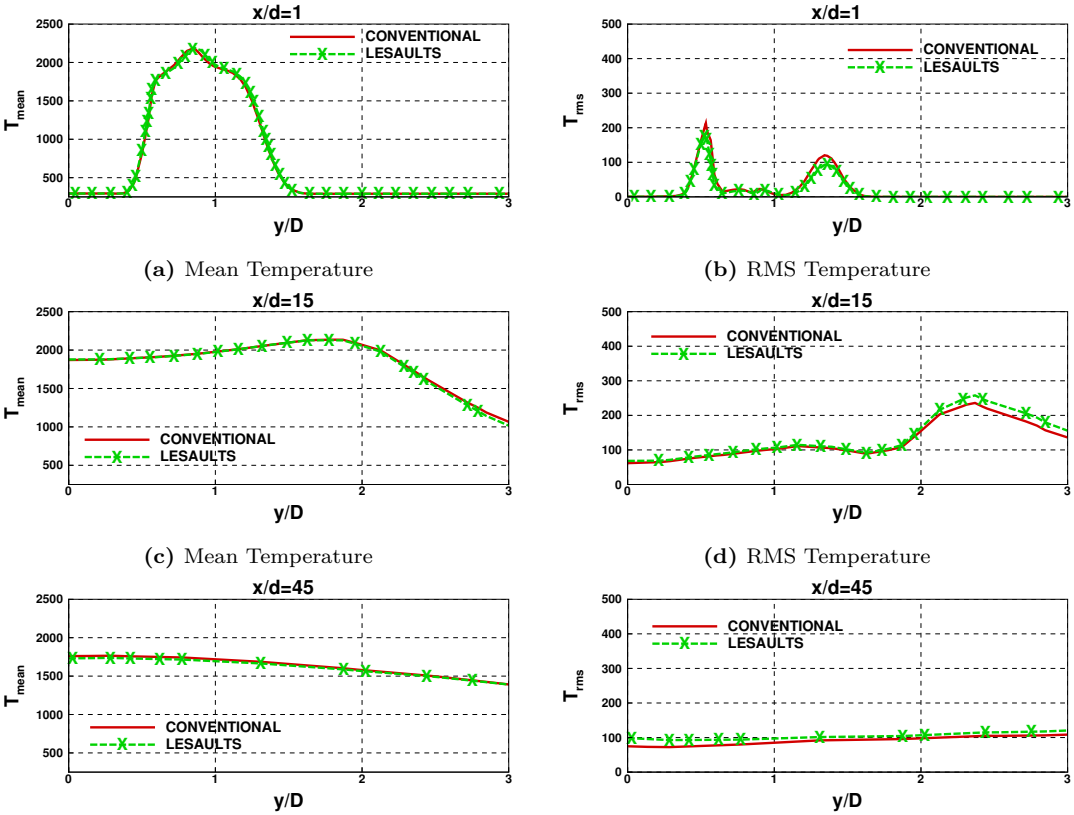

(a) Mean Temperature **(b)** RMS Temperature

(c) Mean Temperature **(d)** RMS Temperature

(e) Mean Temperature **(f)** RMS Temperature

Fig. 26: Radial profiles of mean and rms temperatures plotted at axial downstream planes

90%.

Element type	Scheme	$R_{\delta t,1}$	N_1	N_2	S_{th}	S_{act}	$\eta_{LESAULTS}$
Tetrahedral	LW	4	240738	940311	2.28	2.05	90%

Table 7: Theoretical and actual speedup obtained for the LES of Sandia-D flame

6.3.2. Comparison of results obtained using conventional and LESAULTS method

The results obtained using conventional and LESAULTS method are shown in Figs(26 to 28). The radial profiles of the time-averaged temperature at three axial planes downstream of the fuel jet exit are shown in Fig. 26. The three downstream planes are shown in the Figure and correspond to x/d=1,15 and 45. The mean and rms quantities are calculated by a circumferential averaging of the already time-averaged quantity.

The location of the flame that is anchored at the jet rim can be observed from the radial profile of mean temperature at x/d=1. The two distinct peaks in the rms-temperature, indicating the radial temperature gradient is also pretty evident in Fig. 26 (b). Further downstream, the flame broadening and the flame brush can be observed from Figs. 26(c) and (d). At x/d=45, the plume region of the flame creates a near

uniform radial profile of mean and rms temperature as can be seen in Figs. 26(e) and (f). At all three planes, excellent match is observed between the conventional and LESAULTS results of the mean and rms temperature profiles.

Similar to the temperature plots, profiles of mean mixture fraction and mean species profiles of CH_4, CO and CO_2 are also plotted in Figs. 27 and 28. Similar to the observations made about temperature, excellent match is also observed for the mixture fraction and species profiles asserting the LESAULTS method's ability to reproduce turbulent statistical quantities.

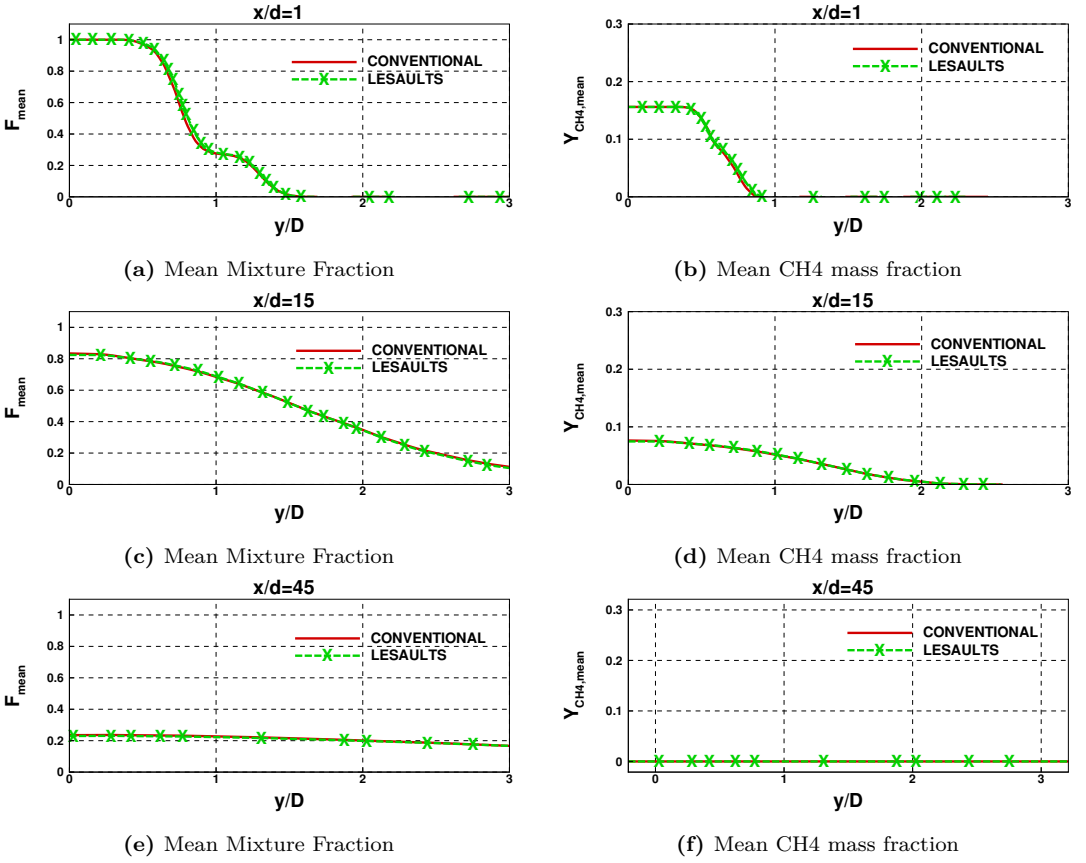

(a) Mean Mixture Fraction **(b)** Mean CH4 mass fraction

(c) Mean Mixture Fraction **(d)** Mean CH4 mass fraction

(e) Mean Mixture Fraction **(f)** Mean CH4 mass fraction

Fig. 27: Radial profiles of mean mixture fraction and CH4 mass fraction plotted at axial downstream planes in the Sandia D flame

7. Conclusions

In this study, a domain decomposition based local time-stepping method is discussed. The method works by decomposing the computational domain into two or more sub-domains with different time steps used in different sub-domains for time integration. The time steps used in each sub-domain are integral multiples of the smallest time step among all sub-domains. Theoretical speedup expressions reveal that the method works well when a relatively smaller groups of cells dictate the smallest time step in a domain. Using global spectral analysis, the size of the overlapped zone is determined and the solution at the overlapped

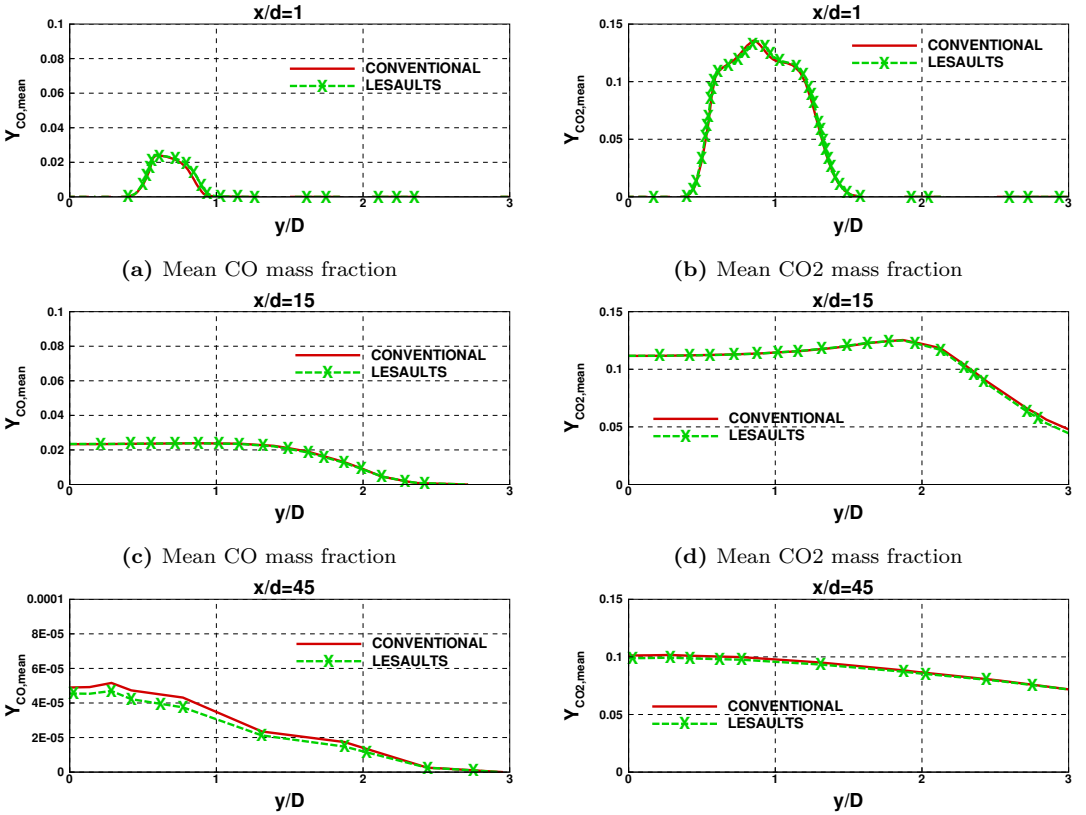

(a) Mean CO mass fraction **(b)** Mean CO2 mass fraction

(c) Mean CO mass fraction **(d)** Mean CO2 mass fraction

(e) Mean CO mass fraction **(f)** Mean CO2 mass fraction

Fig. 28: Radial profiles of CO and CO2 mass fraction plotted at axial downstream planes in the Sandia D flame []

zone is expressed as a weighted combination of the solution sets obtained from the sub-domains. Spectral analysis of the method indicates that the LESAULTS method works as accurately as the conventional method at low to moderate wavenumbers and CFL numbers. The same conclusion also holds as far as the conservation property is concerned. Through a numerical test, it is demonstrated that the order of accuracy of the numerical scheme remains unaffected by LESAULTS method. The method is then validated to work consistently for two numerical schemes (LW and TTGC), cell element types and mesh distributions. LESAULTS method is then applied to the LES of a non-reactive and reactive flow cases. A speedup of more than 100% is obtained for both the cases. LESAULTS method is also demonstrated to accurately reproduce the first and second-order turbulent statistics of these flows.

8. Acknowledgements

The authors would like to thank GENCI-OCCIGEN (Grant 2020-A0052B10157) for the HPC resources used in this study. This study is supported by the IMPROOF (Integrated Model Guided Process Optimization Of Steam Cracking Furnaces) project as a part of the Horizon 2020 framework program of the European Union.

References

[1] U. Piomelli, Large eddy simulations in 2030 and beyond, Philosophical Transactions of the Royal Society A: Mathematical, Physical and Engineering Sciences 372 (2014). doi:10.1098/rsta.2013.0320.

[2] H. Choi, P. Moin, Effects of the computational time step on numerical solutions of turbulent flow, Journal of Computational Physics 113 (1994) 1–4. URL: https://www.sciencedirect.com/science/article/pii/S0021999184711120. doi:https://doi.org/10.1006/jcph.1994.1112.

[3] T. K. Sengupta, V. K. Sathyanarayanan, M. Sriramkrishnan, A. Mulloth, Role of Time Integration in Computing Transitional Flows Caused by Wall Excitation, Journal of Scientific Computing 65 (2015) 224–248. doi:10.1007/s10915-014-9967-1.

[4] Y. Omelchenko, H. Karimabadi, Self-adaptive time integration of flux-conservative equations with sources, Journal of Computational Physics 216 (2006) 179–194. URL: https://www.sciencedirect.com/science/article/pii/S0021999105005619. doi:https://doi.org/10.1016/j.jcp.2005.12.008.

[5] T. Unfer, An asynchronous framework for the simulation of the plasma/flow interaction, Journal of Computational Physics 236 (2013) 229–246. doi:10.1016/j.jcp.2012.11.018.

[6] A. Toumi, G. Dufour, R. Perrussel, T. Unfer, Asynchronous numerical scheme for modeling hyperbolic systems, Comptes Rendus Mathematique 353 (2015) 843–847. URL: https://www.sciencedirect.com/science/article/pii/S1631073X15001740. doi:https://doi.org/10.1016/j.crma.2015.06.010.

[7] T. Unfer, J.-P. Boeuf, F. Rogier, F. Thivet, An asynchronous scheme with local time stepping for multi-scale transport problems: Application to gas discharges, Journal of Computational Physics 227 (2007) 898–918. doi:10.1016/j.jcp.2007.07.018.

[8] T. Unfer, J.-P. Boeuf, F. Rogier, F. Thivet, Multi-scale gas discharge simulations using asynchronous adaptive mesh refinement, Computer Physics Communications 181 (2010) 247–258. doi:10.1016/j.cpc.2009.09.017.

[9] V. Semiletov, S. Karabasov, CABARET scheme for computational aero acoustics: Extension to asynchronous time stepping and 3D flow modelling, International Journal of Aeroacoustics 13 (2014) 321–336. URL: https://doi.org/10.1260/1475-472X.13.3-4.321. doi:10.1260/1475-472X.13.3-4.321. arXiv:https://doi.org/10.1260/1475-472X.13.3-4.321.

[10] T. Unfer, Third order asynchronous time integration for gas dynamics, Journal of Computational Physics 440 (2021) 110434. URL: https://www.sciencedirect.com/science/article/pii/S0021999121003296. doi:https://doi.org/10.1016/j.jcp.2021.110434.

[11] Y. A. Omelchenko, H. Karimabadi, A time-accurate explicit multi-scale technique for gas dynamics, Journal of Computational Physics 226 (2007) 282–300. doi:10.1016/j.jcp.2007.04.010.

[12] M. J. Berger, J. Oliger, Adaptive mesh refinement for hyperbolic partial differential equations, Journal of Computational Physics 53 (1984) 484–512. URL: https://www.sciencedirect.com/science/article/pii/0021999184900731. doi:https://doi.org/10.1016/0021-9991(84)90073-1.

[13] M. Berger, P. Colella, Local adaptive mesh refinement for shock hydrodynamics, Journal of Computational Physics 82 (1989) 64–84. URL: https://www.sciencedirect.com/science/article/pii/0021999189900351. doi:https://doi.org/10.1016/0021-9991(89)90035-1.

[14] L. Krivodonova, An efficient local time-stepping scheme for solution of nonlinear conservation laws, Journal of Computational Physics 229 (2010) 8537–8551. doi:10.1016/j.jcp.2010.07.037.

[15] A. S. Almgren, J. B. Bell, W. Y. Crutchfield, Approximate projection methods: Part I. inviscid analysis, SIAM Journal on Scientific Computing 22 (2000) 1139–1159. URL: https://doi.org/10.1137/S1064827599357024. doi:10.1137/S1064827599357024. arXiv:https://doi.org/10.1137/S1064827599357024.

[16] J. B. Bell, P. Colella, H. M. Glaz, A second-order projection method for the incompressible Navier-Stokes equations, Journal of Computational Physics 85 (1989) 257–283. URL: https://www.sciencedirect.com/science/article/pii/0021999189901514. doi:https://doi.org/10.1016/0021-9991(89)90151-4.

[17] J. Bell, L. Howell, P. Colella, An efficient second-order projection method for viscous incompressible flow, AIAA, 1991, pp. 360–367. URL: https://arc.aiaa.org/doi/abs/10.2514/6.1991-1560. doi:10.2514/6.1991-1560. arXiv:https://arc.aiaa.org/doi/pdf/10.2514/6.1991-1560.

[18] D. Martin, P. Colella, D. Graves, A cell-centered adaptive projection method for the incompressible Navier-Stokes equations in three dimensions, Journal of Computational Physics 227 (2008) 1863–1886. doi:10.1016/j.jcp.2007.09.032.

[19] M. Sussman, A. S. Almgren, J. B. Bell, P. Colella, L. H. Howell, M. L. Welcome, An adaptive level set approach for incompressible two-phase flows, Journal of Computational Physics 148 (1999) 81–124. URL: https://www.sciencedirect.com/science/article/pii/S002199919896106X. doi:https://doi.org/10.1006/jcph.1998.6106.

[20] S. Osher, R. Sanders, Numerical approximations to nonlinear conservation laws with locally varying time and space grids, Mathematics of Computation 41 (1983) 321–336. doi:https://doi.org/10.1090/S0025-5718-1983-0717689-8.

[21] C. Dawson, R. Kirby, High resolution schemes for conservation laws with locally varying time steps, SIAM Journal on Scientific Computing 22 (2001) 2256–2281. URL: https://doi.org/10.1137/S1064827500367737. doi:10.1137/S1064827500367737. arXiv:https://doi.org/10.1137/S1064827500367737.

[22] L. Liu, X. Li, F. Q. Hu, Nonuniform time-step Runge-Kutta discontinuous Galerkin method for computational aeroacoustics, Journal of Computational Physics 229 (2010) 6874–6897. URL: https://www.sciencedirect.com/science/article/pii/S0021999110002895. doi:https://doi.org/10.1016/j.jcp.2010.05.028.

[23] L. Liu, X. Li, F. Q. Hu, Nonuniform-time-step explicit Runge-Kutta scheme for high-order finite difference method, Computers Fluids 105 (2014) 166–178. URL: https://www.sciencedirect.com/science/article/pii/S0045793014003454. doi:https://doi.org/10.1016/j.compfluid.2014.09.008.

[24] O. Knoth, R. Wolke, Implicit-explicit Runge-Kutta methods for computing atmospheric reactive flows, Applied Numerical Mathematics 28 (1998) 327–341. URL: https://www.sciencedirect.com/science/article/pii/S0168927498000518. doi:https://doi.org/10.1016/S0168-9274(98)00051-8.

[25] T.-T.-P. Hoang, W. Leng, L. Ju, Z. Wang, K. Pieper, Conservative explicit local time-stepping schemes for the shallow water equations, J. Comput. Phys. 382 (2019) 152–176. URL: https://doi.org/10.1016/j.jcp.2019.01.006. doi:10.1016/j.jcp.2019.01.006.

[26] A. Sandu, A class of multirate infinitesimal GARK methods, SIAM Journal on Numerical Analysis 57 (2019) 2300–2327. URL: https://doi.org/10.1137/18M1205492. doi:10.1137/18M1205492. arXiv:https://doi.org/10.1137/18M1205492.

[27] G. Jeanmasson, I. Mary, L. Mieussens, On some explicit local time stepping finite volume schemes for cfd, Journal of Computational Physics 397 (2019) 108818. URL: https://www.sciencedirect.com/science/article/pii/S0021999119305029. doi:https://doi.org/10.1016/j.jcp.2019.07.017.

[28] W. Quan, S. Evans, H. Hastings, Efficient integration of a realistic two-dimensional cardiac tissue model by domain decomposition, IEEE Transactions on Biomedical Engineering 45 (1998) 372–385. doi:10.1109/10.661162.

[29] O. Esnault, M. Boileau, R. Vicquelin, B. Fiorina, O. Gicquel, A Method To Accelerate LES Explicit Solvers Using Local Time-Stepping, ????, p. 1. URL: https://arc.aiaa.org/doi/abs/10.2514/6.2010-123. doi:10.2514/6.2010-123. arXiv:https://arc.aiaa.org/doi/pdf/10.2514/6.2010-123.

[30] A. Poubeau, R. Paoli, A. Dauptain, F. Duchaine, G. Wang, Large-eddy simulations of a single-species solid rocket booster jet, AIAA Journal 53 (2015) 1477–1491. URL: https://doi.org/10.2514/1.J053361. doi:10.2514/1.J053361. arXiv:https://doi.org/10.2514/1.J053361.

[31] T. K. Sengupta, A. Dipankar, A comparative study of time advancement methods for solving Navier-Stokes equations, Journal of Scientific Computing 21 (2004) 225–250. doi:https://doi.org/10.1023/B:JOMP.0000030076.74896.d7.

[32] T. K. Sengupta, M. K. Rajpoot, Y. G. Bhumkar, Space-time discretizing optimal DRP schemes for flow and wave propagation problems, Computers Fluids 47 (2011) 144–154. URL: https://www.sciencedirect.com/science/article/pii/S0045793011000818. doi:https://doi.org/10.1016/j.compfluid.2011.03.003.

[33] T. Sengupta, Y. Bhumkar, V. Lakshmanan, Design and analysis of a new filter for LES and DES, Computers Structures 87 (2009) 735–750. URL: https://www.sciencedirect.com/science/article/pii/S0045794908002745. doi:https://doi.org/10.1016/j.compstruc.2008.12.009, fifth MIT Conference on Computational Fluid and Solid Mechanics.

[34] T. K. Sengupta, A. Bhole, N. Sreejith, Direct numerical simulation of 2D transonic flows around airfoils, Computers Fluids 88 (2013) 19–37. URL: https://www.sciencedirect.com/science/article/pii/S0045793013003241. doi:https://doi.org/10.1016/j.compfluid.2013.08.007.

[35] T. K. Sengupta, A. Sengupta, A new alternating bi-diagonal compact scheme for non-uniform grids, Journal of Computational Physics 310 (2016) 1–25. URL: https://www.sciencedirect.com/science/article/pii/S0021999116000152. doi:https://doi.org/10.1016/j.jcp.2016.01.014.

[36] N. Sharma, A. Sengupta, M. Rajpoot, R. J. Samuel, T. K. Sengupta, Hybrid sixth order spatial discretization scheme for non-uniform cartesian grids, Computers Fluids 157 (2017) 208–231. URL: https://www.sciencedirect.com/science/article/pii/S0045793017303225. doi:https://doi.org/10.1016/j.compfluid.2017.08.034.

[37] T. Sengupta, A. Dipankar, A. K. Rao, A new compact scheme for parallel computing using domain decomposition, Journal of Computational Physics 220 (2007) 654–677. URL: https://www.sciencedirect.com/science/article/pii/S0021999106002543. doi:https://doi.org/10.1016/j.jcp.2006.05.018.

[38] T. K. Sengupta, P. Sundaram, V. K. Suman, S. Bhaumik, A high accuracy preserving parallel algorithm for compact schemes for DNS, ACM Trans. Parallel Comput. 7 (2020). URL: https://doi.org/10.1145/3418073. doi:10.1145/3418073.

[39] V. Suman, T. K. Sengupta, C. Jyothi Durga Prasad, K. Surya Mohan, D. Sanwalia, Spectral analysis of finite difference schemes for convection diffusion equation, Computers Fluids 150 (2017) 95–114. URL: https://www.sciencedirect.com/science/article/pii/S0045793017301275. doi:https://doi.org/10.1016/j.compfluid.2017.04.009.

[40] S. Sengupta, T. K. Sengupta, J. K. Puttam, K. S. Vajjala, Global spectral analysis for convection-diffusion-reaction equation in one and two-dimensions: Effects of numerical anti-diffusion and dispersion, Journal of Computational Physics 408 (2020) 109310. URL: https://www.sciencedirect.com/science/article/pii/S002199912030084X. doi:https://doi.org/10.1016/j.jcp.2020.109310.

[41] S. Nadakkal, Large Eddy Simulation of the steam cracking process in refinery furnaces, Ph.D. thesis, INPT, 2022. URL: https://www.theses.fr/s185953, these de doctorat dirigae par Cuenot, Benedicte et Riber, Eleonore Dynamique des fluides Toulouse, INPT 2022.

[42] P. Lax, B. Wendroff, Systems of conservation laws, Communications on Pure and Applied Mathematics 13 (1960) 217–237. URL: https://onlinelibrary.wiley.com/doi/abs/10.1002/cpa.3160130205. doi:https://doi.org/10.1002/cpa.3160130205. arXiv:https://onlinelibrary.wiley.com/doi/pdf/10.1002/cpa.3160130205.

[43] O. Colin, M. Rudgyard, Development of high-order Taylor-Galerkin schemes for LES, Journal of Computational Physics 162 (2000) 338–371. URL: https://www.sciencedirect.com/science/article/pii/S0021999100965380. doi:https://doi.org/10.1006/jcph.2000.6538.

[44] T. Sengupta, High Accuracy Computing Methods: Fluid Flows and Wave Phenomena, Cambridge University Press, 2013. doi:10.1017/CBO9781139151825.

[45] T. Schonfeld, M. Rudgyard, Steady and unsteady flow simulations using the hybrid flow solver AVBP, AIAA Journal 37 (1999) 1378–1385. URL: https://doi.org/10.2514/2.636. doi:10.2514/2.636. arXiv:https://doi.org/10.2514/2.636.

[46] X. Ma, G.-S. Karamanos, G. E. Karniadakis, Dynamics and low-dimensionality of a turbulent near wake, Journal of Fluid Mechanics 410 (2000) 29–65. doi:10.1017/S0022112099007934.

[47] S. Dong, G. E. Karniadakis, A. Ekmekci, D. Rockwell, A combined direct numerical simulation particle image velocimetry study of the turbulent near wake, Journal of Fluid Mechanics 569 (2006) 185–207. doi:10.1017/S0022112006002606.

[48] R. Mittal, P. Moin, Suitability of upwind-biased finite difference schemes for large-eddy simulation of turbulent flows, AIAA Journal 35 (1997) 1415–1417. URL: https://doi.org/10.2514/2.253. doi:10.2514/2.253. arXiv:https://doi.org/10.2514/2.253.

[49] G. Deng, J. Piquet, P. Queutey, M. Visonneau, Vortex-shedding flow predictions with eddy-viscosity models, in:

W. RODI, F. MARTELLI (Eds.), Engineering Turbulence Modelling and Experiments, Elsevier, Oxford, 1993, pp. 143–152. URL: https://www.sciencedirect.com/science/article/pii/B9780444898029500204. doi:https://doi.org/10.1016/B978-0-444-89802-9.50020-4.

[50] C. Jared S., R. Christopher L., B. Kenneth S., Y. Bassam A., Computation of Sound Generated by Viscous Flow Over a Circular Cylinder, Technical Report, 1997.

[51] L. Ong, J. Wallace, The velocity field of the turbulent very near wake of a circular cylinder, Experiments in Fluids 20 (1996) 441–453. doi:10.1007/BF00189383.

[52] A. G. Kravchenko, P. Moin, Numerical studies of flow over a circular cylinder at $\mathrm{Re_D}$=3900, Physics of Fluids 12 (2000) 403–417. URL: https://doi.org/10.1063/1.870318. doi:10.1063/1.870318. arXiv:https://doi.org/10.1063/1.870318.

[53] B. N. Rajani, A. Kandasamy, S. Majumdar, LES of flow past circular cylinder at Re = 3900, Journal of Applied Fluid Mechanics 9 (2016) 1421–1435. doi:10.18869/acadpub.jafm.68.228.24178.

[54] F. Nicoud, H. B. Toda, O. Cabrit, S. Bose, J. Lee, Using singular values to build a subgrid-scale model for large eddy simulations, Physics of Fluids 23 (2011) 085106. URL: https://doi.org/10.1063/1.3623274. doi:10.1063/1.3623274. arXiv:https://doi.org/10.1063/1.3623274.

[55] T. Jaravel, E. Riber, B. Cuenot, P. Pepiot, Prediction of flame structure and pollutant formation of Sandia flame D using large eddy simulation with direct integration of chemical kinetics, Combustion and Flame 188 (2018) 180–198. URL: https://www.sciencedirect.com/science/article/pii/S0010218017303504. doi:https://doi.org/10.1016/j.combustflame.2017.08.028.

[56] B. Franzelli, E. Riber, B. Cuenot, Impact of the chemical description on a large eddy simulation of a lean partially premixed swirled flame, Comptes Rendus Mecanique 341 (2013) 247–256. URL: https://www.sciencedirect.com/science/article/pii/S163107211200215X. doi:https://doi.org/10.1016/j.crme.2012.11.007, combustion, spray and flow dynamics for aerospace propulsion.

[57] O. Colin, Simulations aux grandes Eschelles de la combustion turbulente prolongee dans les stator-acteurs, Ph.D. thesis, INPT, 2000. URL: http://www.theses.fr/2000INPT011H, thee de doctorat dirigage par Poinsot, Thierry Mecanique DES fluides Toulouse, INPT 2000.

Appendix A. Global Spectral Analysis of LW and TTGC Schemes

Let us consider the numerical solution of the given LCE expressed in Eq. 17 on a periodic domain. Let u_i^n denote the numerical solution of the equation at the ith node and at time level n. The location of the ith node is given by $x_i = i\,h$ where h is the grid spacing. The current numerical time $t^n = n\,\Delta t$ where Δt is the time step used. The numerical value of u at time $n+1$ is given by the general expression for explicit time integration schemes as,

$$u_i^{n+1} = S(u_{i-l}^n, u_{i-l+1}^n \dots u_{i+m}^n - 1, u_{i-l}^{n-1}, u_{i-l+1}^{n-1} \dots u_{i+m}^{n-1}, \dots u_{i-l}^{n-p}, u_{i-l+1}^{n-p} \dots u_{i+m}^{n-p}) \tag{A.1}$$

where l and m depend on the spatial stencil chosen and p depends on the temporal integration scheme. The Fourier transform of the numerical solution at node j and time level n can be expressed as,

$$u_j^n = \int \hat{U}(k, t^n)\, e^{i\,k\,x_j}\, dk, \tag{A.2}$$

The Fourier transform of u_{j+l}^n then becomes using the phase shift property,

$$u_{j+l}^n = \int \hat{U}(k, t^n)\, e^{i\,k\,x_j} e^{i\,k\,lh}\, dk, \tag{A.3}$$

In analogy to the governing PDE, u_j^{n+1} is expressed as

$$u_j^{n+1} = \int G_{num} \hat{U}(k, t^n)\, e^{i\,k\,x_j}\, dk, \tag{A.4}$$

where G_{num} is the numerical amplification factor, which may be written as

$$G_{num} = \frac{\hat{U}(k, t^n + \Delta t)}{\hat{U}(k, t^n)} \tag{A.5}$$

The numerical dispersion relation is then be expressed as,

$$\omega_{num} = c_{num}\, k \tag{A.6}$$

where ω_{num} and c_{num} are the numerical phase speed and circular frequency respectively. Unlike the physical circular frequency ω, the numerical circular frequency will be a complex function when there are central difference terms occurring. The numerical phase angle β is given by,

$$tan(\beta) = -\left(\frac{(G_{num})_{Imag}}{(G_{num})_{Real}}\right) \tag{A.7}$$

$(G_{num})_{Imag}$ and $(G_{num})_{Real}$ are the imaginary and real parts of the complex quantity G_{num}.

The numerical phase speed c_{num} is then obtain as,

$$c_{num} = \frac{\omega_{num}}{k} = \frac{\beta}{k\,\Delta t} \tag{A.8}$$

leading to the definition of the normalised numerical phase speed,

$$\frac{c_{num}}{c} = \frac{\beta}{kh\, N_c} \tag{A.9}$$

where N_c is the Courant-Friedlich-Lewy (CFL) number defined by $N_c = c\Delta t/h$.

The group velocity of the numerical solution $V_{g,num}$ is then calculated as,

$$V_{g,num} = \frac{\partial \omega_{num}}{\partial k} = \frac{1}{\Delta t}\,\frac{\partial \beta}{\partial k} \tag{A.10}$$

leading to the definition of the normalised numerical group velocity,

$$\frac{V_{g,num}}{c} = \frac{\partial \beta}{N_c\, \partial kh} \tag{A.11}$$

The before mentioned analysis is general for any numerical scheme. The application of this analysis to LW and TTGC schemes are provided in the following sections.

Appendix A.0.1. Application to LW and TTGC Schemes

The LW scheme when applied to the 1D LCE on a uniform grid with grid spacing h and time step Δt and CFL number N_c is given as follows:

$$u_j^{n+1} = u_j^n - \frac{N_c}{2}(u_{j+1}^n - u_{j-1}^n) + \frac{N_c^2}{2}(u_{j+1}^n - 2u_j^n + u_{j-1}^n), \tag{A.12}$$

Applying the spectral analysis as discussed previously to this stencil, gives the following relations for the amplification factor (G_{LW}) for the LW scheme.

$$G_{LW} = 1 - i\, N_c sin(kh) + [N_c^2(cos(kh) - 1)]. \tag{A.13}$$

The relations for the numerical phase speed and group velocity then follow using the analysis shown before as,

$$\frac{c_{num}}{c} = \frac{1}{(kh)N_c} tan^{-1}\left(\frac{N_c\, sin(kh)}{1 + N_c^2(cos(kh) - 1)}\right). \tag{A.14}$$

$$\frac{v_{g,num}}{c} = \left[\frac{cos(kh) + N_c^2(1 - cos(kh))}{\left(1 + N_c^2(cos(kh) - 1)\right)^2 + N_c^2\, sin^2(kh)}\right]. \tag{A.15}$$

The TTGC scheme is derived ([43]) similar to the LW scheme by employing Taylor series expansion of u with respect to time and substituting the first and second-order time derivatives using central spatial difference relations. The scheme is designed to involve two steps and when applied to LCE is given as,

$$\tilde{u}^n = u^n + \alpha_{TTGC}\, \Delta t u_t^n + \beta_{TTGC} \Delta t^2\, u_{tt}^n \tag{A.16}$$

$$u^{n+1} = u^n + \Delta t \tilde{u_t}^n + \gamma_{TTGC} \Delta t^2\, u_{tt}^n$$

where $\tilde{()}$ denotes the values of the numerical solution at the intermediate time step. α_{TTGC},β_{TTGC} and γ_{TTGC} are tunable constants. Applying the Galerkin approach assuming P1 element formulation one obtains,

$$\frac{(\tilde{u}^n_{i+1} + 4\tilde{u}^n_i + \tilde{u}^n_{i-1})}{6} = \frac{(u^n_{i+1} + 4u^n_i + u^n_{i-1})}{6} - \alpha_{TTGC}\, N_c \frac{(u^n_{i+1} - u^n_{i-1})}{2} \tag{A.17}$$

$$+ \beta_{TTGC}\, N_c^2\, (u^n_{i+1} - 2u_i + u^n_{i-1}) \tag{A.18}$$

$$\frac{(u^n_{i+1} + 4u^n_i + u^n_{i-1})}{6} = \frac{(u^n_{i+1} + 4u^n_i + u^n_{i-1})}{6} - N_c \frac{(\tilde{u}^n_{i+1} - \tilde{u}^n_{i-1})}{2} \tag{A.19}$$

$$+ \gamma_{TTGC}\, N_c^2\, (u^n_{i+1} - 2u_i + u^n_{i-1}) \tag{A.20}$$

Applying the previously mentioned analysis on the above stencil, one obtains the expressions for the amplification factor for TTGC scheme G_{TTGC}, the phase speed and group velocity as given below.

$$G_{TTGC} = 1 + \gamma_{TTGC} N_c \hat{A}\hat{S} - \alpha_{TTGC}(\hat{A}\hat{L})^2 - i\hat{A}\hat{L}\left(1 + \beta_{TTGC} N_c \hat{A}\hat{S}\right) \tag{A.21}$$

$$\frac{c_{num}}{c} = -\frac{\theta}{(kh)N_c} \tag{A.22}$$

$$\frac{V_{g,num}}{c} = \frac{1}{N_c}\frac{\partial\theta}{\partial kh} \tag{A.23}$$

Here, θ is the argument of the complex function G_{TTGC}. The parameters in Equation A.23 are defined as,

$$\hat{A} = \frac{3\, N_c}{(2 + cos(kh))}, \tag{A.24}$$

$$\hat{S} = 2\,(cos(kh) - 1) \tag{A.25}$$

$$\hat{L} = sin(kh) \tag{A.26}$$